Engineering Structures 330 (2025) 119928

Contents lists available at ScienceDirect

Engineering Structures

journal homepage: www.elsevier.com/locate/engstruct

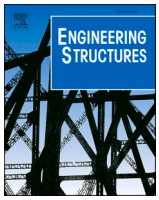

Waterborne debris impact forces on wall structures: Elastic analytical model integrating the effects of the structural mass

Alessandro De Iasio [a,*], Bahman Ghiassi [b], Riccardo Briganti [a], Gabriele Milani [c]

[a] Faculty of Engineering, University of Nottingham, Nottingham NG7 2RD, UK
[b] School of Engineering, University of Birmingham, Birmingham B15 2TT, UK
[c] Department of Architecture Built Environment and Construction Engineering (ABC), Politecnico di Milano, Piazza Leonardo da Vinci 32, Milan 20133, Italy

ARTICLE INFO

Keywords:
Extreme hydrodynamic events
Debris impact
Structural mass
Analytical model
Force-time diagram

ABSTRACT

To evaluate the structural safety against waterborne debris impacts, the impact loads are usually computed with analytical models such as those proposed by ASCE/SEI 7–22. These models often assume a massless structure to simplify the analytical formulations, which can be an oversimplifying and inaccurate assumption in cases where the structure is heavier and more flexible than the debris. To address this problem, we aim to define the domain in which the existing models are inaccurate and to propose a new analytical model to accurately compute the debris impact forces through comprehensive finite element simulations and analytical modelling. We defined such a domain in the design space of structure-to-debris mass and stiffness ratios and assessed which are the most accurate analytical models to compute debris impact forces across this space. Our proposed model significantly improves upon the overestimating results of the ASCE/SEI 7–22 model when both stiffness and mass are important in determining the impact forces.

1. Introduction

Waterborne debris impacts during extreme hydrodynamic events, such as tsunamis or floods, can cause significant structural damage, also as repeated impacts [25]. Their accurate consideration in structural assessments in flood and tsunami-prone areas is fundamental [35]. Debris impacts are typically represented by force-time (F-t) diagrams used in structural simulations to model equivalent impact forces, e.g. in [15] or [7]. Therefore, correct calculations of such diagrams are important to obtain reliable structural simulations.

Previous experimental and numerical works studied the F-t diagrams of uniform bar-like debris, like logs, impacting on structures [13,26,28]. All these studies assumed elastic impacts i.e. both the debris and the structure behave elastically during the impact. The debris hits the structure orthogonally to maximise the peak impact force. Debris have impact velocity v_d, mass m_d and stiffness k_d. Structures have stiffness k_s. The structural mass m_s is neglected. The stiffness k_d is associated with the axial bar stiffness, while k_s with the structure stiffness at impact location. These studies give the base for the existing analytical models to calculate debris impacts F-t diagrams, including the design formulae by ASCE/SEI 7–22 [2]. The F-t diagrams depend on the debris-structure interaction: the impact load is more severe as v_d and m_d increase because they increase the debris momentum, and as k_d increases because it decreases the shock wave absorption provided by debris deformations. Impact loads are also more severe as k_s increases because it increases the resistance opposed by the structure to the debris. A high or low structural resistance determines the occurrence of rigid or flexible impacts, respectively. An impact is rigid if the structure behaves as a rigid body, i.e. it does not move appreciably under debris actions. Otherwise, the impact is flexible. This is governed by the structure-to-debris stiffness ratio δ (Eq. 5) [26]. Flexible impacts occur for $\delta < 1$ and rigid impacts for $\delta > 5$, intermediates responses are observed for the inner values. The shape of the F-t diagram is rectangular in rigid impacts and sinusoidal in flexible impacts.

However, [6] recently revealed the critical role of m_s in debris impacts. They demonstrate that, m_s becomes highly important when the structure-to-debris mass ratio μ (see Eq. 5) exceeds a critical value, μ_{cr}, and the impact is not rigid ($\delta < 5$). Here, m_s determines a shift in the F-t diagrams as rectangular F-t diagrams with force values proportional to μ, are generated in place of the sinusoidal diagrams with less severe loading rate and peak force calculated neglecting m_s. Furthermore, [6] showed that existing analytical models to compute the F-t diagrams of debris impacts, including the design formulae by ASCE/SEI 7–22, are

* Corresponding author.
E-mail addresses: alessandro.deiasio@nottingham.ac.uk (A. De Iasio), b.ghiassi@bham.ac.uk (B. Ghiassi), riccardo.briganti@nottingham.ac.uk (R. Briganti), gabriele.milani@polimi.it (G. Milani).

https://doi.org/10.1016/j.engstruct.2025.119928
Received 11 October 2024; Received in revised form 15 January 2025; Accepted 10 February 2025

Nomenclature

a_i	mesh node acceleration
A_d	debris cross-section area
$A_{1,2,3,4}$	coefficients of the best-fitting curves in the MSRM
b_s	structure thickness
c	wave speed in solids
c_{1D}	wave speed in solids in a one dimension
D_{m_s}	importance domain of m_s
δ	structure-to-debris stiffness ratio
δ_{cr}	critical stiffness ratio
E_d	debris Youngs' modulus
E_s	structure Youngs' modulus
ε_{Fh}	error for F_h
ε_{td}	error for t_d
ε_I	error for I
ε_u	error for $u_{\max}$
F	impact force
F_h	general plateau force in the rectangular F-t diagrams
F_m	inertia force
F_p	spike peak force
Fr	Froude number
φ_d	debris diameter
h_w	water depth
H_s	wall structure height
I	impulse of the F-t diagram
k_d	debris stiffness
k_s	structure stiffness
L_d	debris length
L_s	square plate edge length
m_d	debris mass
m_s	structure mass
m_i	FE model nodal lumped mass
μ	structure-to-debris mass ratio
μ_{cr}	critical mass ratio
ν_d	debris Poisson's ratio
ν_s	structure Poisson's ratio
p	vertical external linear load
q_w	horizontal water flow pressure
R	horizontal reaction force
ρ_d	debris density
ρ_s	structure density
t	time
t_d	impact duration
t_p	spike time
θ_I	F-t diagram impulse variation
u	horizontal structural displacement
$u_{\max}$	maximum structural displacement
v_d	debris impact velocity

Acronyms

ASCE	American Society of Civil Engineers
bc	structure boundary conditions
SW	Self-Weight
1DWP	One-Dimensional Wave Propagation model
MSRM	Mass and Stiffness Ratios model

significantly inaccurate when m_s is important. These findings apply to many realistic debris impact scenarios involving brick masonry, concrete and cross-layered wooden panels (XLAM) walls. However, two significant research gaps were not addressed in the cited article. First, the critical thresholds of μ and δ for which m_s becomes highly important are not defined, as well as their possible relationships with other factors such as vertical and horizontal loads and boundary conditions. Second, there is a lack of analytical models that correctly integrate the effect of m_s in calculating debris impact F-t diagrams

In this paper, we aim to define the domain D_{m_s} in the $\mu-\delta$ space where the m_s is important and propose a new analytical model, the Mass and Stiffness Ratios Model (MSRM), for calculating the F-t diagrams of elastic impacts accounting for the effects of m_s in that domain. The boundaries of D_{m_s} are defined using critical structure-to-debris mass and stiffness ratios. The influence of self-weight, vertical and horizontal loads and boundary conditions on D_{m_s} is also assessed. The MSRM is finally compared with the ASCE model in realistic case studies. The data needed to achieve these objectives are collected with validated Finite Element (FE) simulations. The hypotheses of elastic and orthogonal impacts are maintained to align with previous literature and isolate the effects of m_s, aiming at investigating their effects in future studies. We focus on log debris impacts in line with most existing literature [21], aiming to investigate the possible generalization of the presented results to other debris typologies like cars or shipping containers in future studies.

2. Methodology

The results of this paper are obtained with validated numerical models. The domain D_{m_s} is assessed by investigating the F-t diagrams of different impact scenarios in a wide range of structure-to-debris mass and stiffness ratios μ and δ, respectively. The influence of vertical and horizontal loads and boundary conditions is studied by analysing the sensitivity of the F-t diagrams to these factors. The MSRM is developed from the general trends of the F-t diagrams across the $\mu-\delta$ space within D_{m_s}.

2.1. Finite element impact models

As explained above, the impact scenario is that of a log debris colliding with a structure. This is simulated using Finite Element (FE) analyses run with the commercial software Abaqus/Explicit [1]. Two different impact models are used: the solid debris impact model (Fig. 1-a) and the equivalent impact force model (Fig. 1-b). The former is a validated strategy where both debris and structure are modelled. It is used to collect the reference results because it accurately replicates the debris-structure interaction [6]. The latter is the common strategy for structural analyses for debris impacts (see Section 1), where only the structure is modelled and the debris action is introduced using an equivalent impact F-t diagram. This approach is used to assess the accuracy of the applied F-t diagrams by comparing its results with the related solid debris impact model.

In the solid debris impact model, the log debris is idealised as a uniform bar with length L_d, circular cross-section area A_d, Young's modulus E_d and density ρ_d. The impact is orthogonal to the wall with impact area A_d, which is the worst-case scenario for the peak impact force (see Section 1). Elastic impacts are assumed to align with the existing literature and isolate the effects of m_s (see Section 1). This hypothesis is valid if debris impacts do not lead to structural damage. However, post-disaster surveys highlight that structural damage can occur under debris impacts (see Section 1). Therefore, investigating impact nonlinearities is an important future research topic to increase the applicability of this study to a broader number of impact scenarios. Regarding the high strain rate effects, [7] demonstrated that high strain rate effects in debris impact scenarios are important only for the post-elastic material properties, e.g. the tensile strength, while they do not influence the elastic response of the material, e.g. the Youngs' modulus. De Iasio et al. [7] also show that this is valid for broad

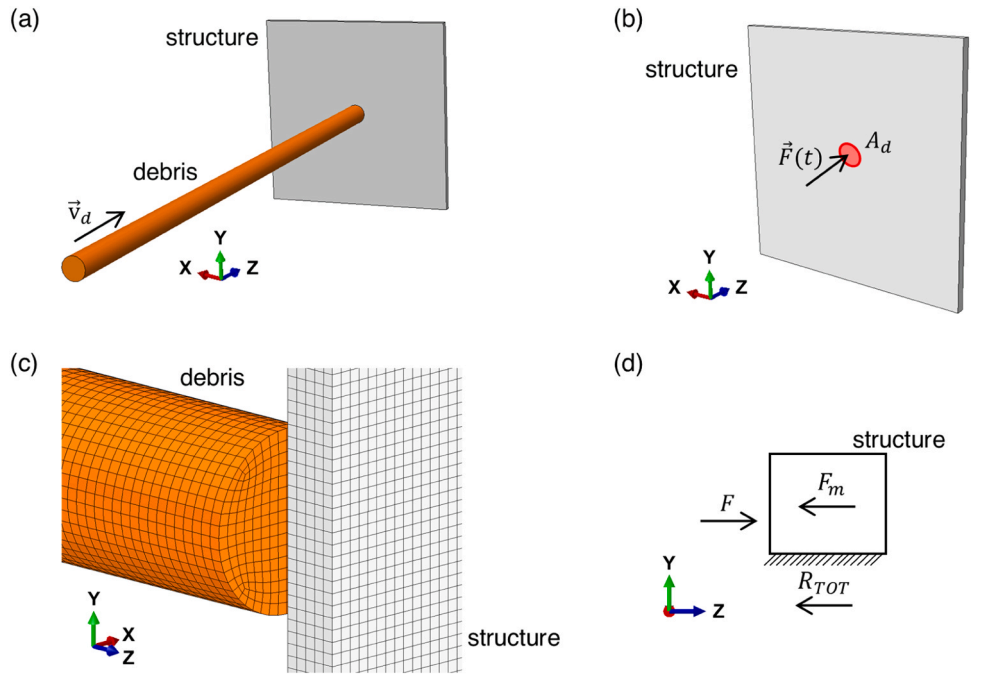

Fig. 1. (a) Solid debris and (b) equivalent force impact models. (c) Finite Elements mesh. (d) Scheme of the main horizontal forces acting on the structure.

scenarios of debris impacts, including different impact velocities. Therefore, high strain rate effects are not considered in this study as elastic materials are considered. The natural radial variability of structural properties in logs is neglected aligning with validated past studies, which characterised the logs stiffness with a global axial stiffness (see Section 1). Also, a central symmetry of these properties is expected at the impact head given the impact orthogonality, which further supports the assumption of a global idealised axial stiffness. An influence of this detail may be expected in non-orthogonal impacts, where the impact head would have non-symmetrical mechanical properties. However, non-orthogonal impacts are out of the scope of this study and will be investigated in future studies. Moreover, the roughness of the structure is also neglected by modelling the structure surface as perfectly flat. This makes the debris-structure interface equal to the debris cross-section. An influence of this debris-structure interface may be expected, but its analysis is out of the scope of this study and will be carried out in future studies. No damping is implemented as negligible for the structural response under impact loads [4]. The General Contact algorithm [1] is used to model the contact between debris and structure. The default penalty stiffness is chosen to optimise the stable time increment of the explicit simulation [1]. The numerical F-t diagrams are evaluated by taking F as the total contact force.

The effects of the surrounding water between the debris and the structure, which influence the debris impacts F-t diagrams [14], are not considered since the fluid phase is not modelled. However, these effects are expected to be limited if the cross-section area of the debris is small, as in the case of log debris [26]. This allows to present reliable results on log debris impacts. Nevertheless, future dedicated research should focus on how the surrounding water effects interact with the m_s effects, particularly for debris with larger cross-sections such as shipping containers or cars.

The mesh consists of linear hexahedral elements with full integration (C3D8) (Fig. 1-c). Only linear hexahedral elements are allowed by Abaqus Explicit [1]. In the meantime, the full integration removes the Hourglass effects typical of dynamic simulations. The finite elements are cubes of similar sizes. Furthermore, in the equivalent impact force model, the structure is the same and the F-t diagrams are described with a function $F(t)$ implemented as uniform pressure loads over an area equal to the cross-section area A_d.

Finally, to clarify the reasons behind the effects of m_s, a comprehensive physical explanation is provided in terms of inertia forces and elastic stress waves propagation in the structure. The related discussions are complementary. Inertia forces in the structure are evaluated using a lumped mass approach. Applying Newton's Second Law, the total horizontal inertia force $F_m(t)$ is computed as:

$$F_m(t) = \sum_{i=1}^{n} a_i(t) m_i \tag{1}$$

where $a_i(t)$ is the horizontal acceleration and m_i the lumped mass for the i^{th} node of the structure mesh, and n is the total number of nodes. The value of m_i is the same for every node because the mesh has cubic elements of similar sizes. As such, $m_i = M/n$ and Eq. 1 becomes:

$$F_m(t) = m_i \sum_{i=1}^{n} a_i(t) \tag{2}$$

The dynamic horizontal equilibrium equation [4] for the structure is:

$$F(t) - R_{TOT}(t) - F_m(t) = 0 \tag{3}$$

where $R_{TOT}(t)$ is the total horizontal reaction force, and the directions of the forces, schematised in Fig. 1-d, are defined as in classical mechanics. The m_s-dependent impact force is explained by analysing F_m in relation to the mass ratio μ (see Eq. 5), and consequently the structural mass m_s. In presenting the results, R_{TOT} and F_m are non dimensionalised as done for F (see Eq. 6).

Moreover, the stress waves are discussed by considering their propagation in the structure from the impact location. Elastic waves propagate in solids at speed c computed as [18]:

$$c = \sqrt{\frac{E_s}{\rho_s} \frac{1-\nu_s}{(1-2\nu_s)(1+\nu_s)}} \tag{4}$$

Eq. 4 links c and the mass ratio μ, which is among the fundamental parameters that define the investigated impact scenarios (see Eq. 5). Indeed, μ is proportional to m_s, which is proportional to ρ_s. As such, c and μ are inversely proportional, allowing to discuss the role of m_s in light of c. The values of R and horizontal displacements u are shown to demonstrate this.

2.2. Numerical simulations programme

2.2.1. Definition of D_{m_s}

The domain D_{m_s} where m_s is important is defined in the $\mu - \delta$ space as $D_{m_s} : (\mu_{cr}, \ +\infty) \cup (0, \delta_{cr})$, where μ_{cr} and δ_{cr} are the critical mass and stiffness ratios, respectively, defining the boundaries of D_{m_s}. The ratios μ and δ are associated with each impact scenario and computed as:

$$\mu = \frac{m_s}{m_d}, \ \delta = \frac{k_s}{k_d} \tag{5}$$

where $m_s = V_s\rho_s$ and $m_d = V_d\rho_d$. The terms V_s and V_d are the structure and debris volumes, and ρ_s and ρ_d the structure and debris densities, respectively. The value of the debris stiffness k_d is calculated as $k_d = E_dA_d/L_d$ [26]. The value of structural stiffness k_s is calculated as the ratio between an arbitrary force applied at the impact point and the displacement caused by this force along the impact direction. A main dataset of F-t diagrams with 143 combinations of μ and δ is defined. Realistic values of μ and δ are taken from a wide database of realistic impact scenarios as in [6]. The rationale behind the definition of this database is presented in Appendix A. The values of μ are 0.001, 0.1, 0.5, 1, 2, 5, 7, 10, 20, 40, 60, 80 and 100, while those of δ are 0.05, 0.1, 0.2, 0.4, 0.6, 0.8, 1, 2, 3, 4 and 5. The μ lower bound is chosen to comply with the massless structure assumption [6] and get references to identify the effects of m_s. The μ upper bound and δ lower bound are chosen as realistic limits[6]. Finally, higher values of δ are unnecessary since m_s has no effects in rigid impacts (see Section 1). Only the debris action is considered to isolate the effects of m_s. This is also in line with ASCE/SEI 7–22 that do not require such loads to be combined with other actions.

The values of μ_{cr} and δ_{cr} are identified comparing the numerical F-t diagrams with the analytical diagrams calculated with the flexible solutions of the 1DWP model, i.e. the flex1DWP (see Appendix B), which is accurate to calculate debris impact forces on massless structures [6]. As such, the m_s effects on the numerical F-t diagrams can be directly observed. This comparison is carried out qualitatively, in terms of F-t diagrams shapes and values, and quantitatively using the error ε_{td}. This error is calculated as the duration of the numerical F-t diagram with respect to that of the analytical F-t diagrams and used as a meaningful metric to quantify the difference between such numerical and analytical diagrams. A ±5% error band is considered for ε_{td} to individuate significant differences between the numerical and analytical diagrams. The rigid solution of the 1DWP model, i.e. the rigid1DWP, is also shown to support data comparison, while the model by ASCE/SEI 7–22, i.e. the ASCE model, is reported as a useful reference of the current design practice. Appendix B describes these models. As in [6], impact forces are normalised to generalise the results. As such, the nondimensional F-t diagrams are presented through the parameters F_{nodim} and t_{nodim}, which are calculated from the output F and t, respectively, normalised as:

$$F_{nodim} = \frac{F}{v_d\sqrt{m_dk_d}}, \quad t_{nodim} = \frac{t}{2\sqrt{m_d/k_d}} \tag{6}$$

The F-t diagrams are collected using a solid debris impact model (see Section 2.1). This model can represent a generic impact scenario involving wall structures and debris with different geometry, boundary conditions and mechanical properties, provided that the values of μ and δ are maintained. This is a fundamental property of the used impact model, which is demonstrated in Appendix C by showing that the simulations result in similar F-t diagrams when varying the structure geometry and boundary conditions, or debris geometry, while maintaining μ and δ. As a meaningful example, Appendix C also shows that this model can replicate the debris impact scenario for a real masonry wall by maintaining μ and δ. These values are maintained by adapting the structure or debris properties in the impact model. Therefore, establishing the general validity of this impact model, the structure and debris geometrical and mechanical properties do not need to be realistic values but only lead to realistic values of μ and δ. These values are extracted considering realistic structural properties collected in Table A1 (see Appendix A).

In this work, we fixed the debris properties as the minimum design demand imposed by ASCE/SEI 7–22. Meanwhile, we fixed the structure geometry and boundary conditions and varied the structure mechanical properties to get the required values of μ and δ. The debris properties are $m_d = 450kg$ and $k_d = 61300kN/m$ and correspond to $L_d = 9m$, diameter $\varphi_d = 0.3m$, $\rho_d = 690kg/m^3$ and $E_d = 7580MPa$. The debris Poisson's ratio is $\nu_d = 0.3$ as typical for wood [17]. The impact velocity is $v_d = 1.78m/s$ following the realistic hydraulic scenario of [7]. The structure is a square plate with edge $L_s = 3m$ and thickness $b_s = 0.1m$, simply supported on all the edges (i.e. boundary condition #1 in Fig. A1, see Appendix A). The values of ρ_s and E_s are adapted in each simulation to obtain the needed values of μ and δ. The structure Poisson's ratio $\nu_s = 0.2$, as typical of common materials such as concrete or masonry. The log impacts the structure at its centre, i.e. at $1.5m$ from the bottom and lateral edges. De Iasio [6] present an extensive mesh sensitivity analysis, demonstrating that mesh independent results are achieved in a broad range of mesh dimensions between $5mm$ and $30mm$. In this study, which uses the same modelling methodology as [6], a mesh size equal to $20mm$ is set to limit the computational effort while maintaining a dense mesh to calculate the inertia forces F_m for a sufficiently high number of nodes (see Eq. 2).

2.2.2. Presence of additional factors in real impact scenarios

Additional factors are also present in real impact scenarios, such as self-weight, vertical external actions and horizontal water flow loads. Boundary conditions are also variable. Their influence on D_{m_s} is investigated for significant values of μ and δ defined in Section 3.2 following the results of Section 3.1. These factors, applied independently to isolate their effects and compared with the results of the main dataset as reference, are defined as follows:

1. The self-weight SW is implemented as a gravity body load.
2. The external vertical loads p are linear loads acting at the top edge meant to represent roof or upper stories loads (Fig. 2). Two different values of p are used, i.e. $p_1 = 37.76kN/m$ and $p_2 = 13.19kN/m$, as typical for residential two-storey buildings [16].
3. The horizontal water flow loads q_w are pressure loads acting on the wall surface representing the flow forces acting on structures during extreme hydrodynamic events (Fig. 2). In line with previous literature on extreme hydrodynamic events, the flow is assumed in steady state and compatible with the shallow water approximation [16,27,30]. These conditions allow to characterise the flow regime using the well-known Froude number $Fr = v_w/\sqrt{gh_{h_w}}$, with v_w being the flow velocity, h_w the flow depth and g the gravity acceleration. A subcritical flow ($Fr \leq Fr_c$, with Fr_c being the critical value) regime is used as a common realistic condition [27]. Subcritical flows are

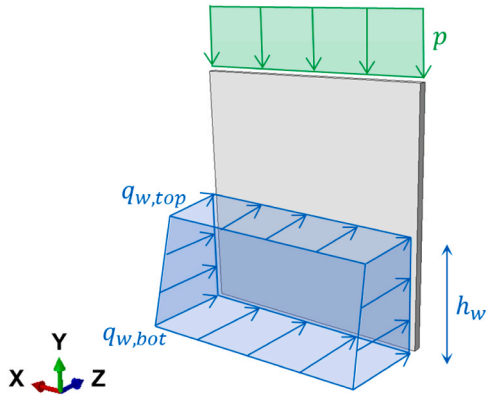

Fig. 2. Modelling of horizontal water flow loads and vertical external loads.

associated to Fr lower than critical values Fr_c. A sparse environment is assumed, which leads to $Fr_c = 1$ [30]. Moreover, the steady flow state allows to consider quasi-static fluid pressures in line with existing literature, e.g. [15], Petrone et al. (2017) and Jansen et al. (2020). This choice implies that flow variability in space and time is not considered. The structural damage associated with flow pressures [20] could still be identified even with such a quasi-static load definition. However, this damage is not considered since elastic materials are used under the assumption of elastic impacts (see Sections 1 and 2.1). Investigating the effects of non-quasi-static flow load definition and the associated damage on the debris impact force is out of the scope of this paper and will be examined in future studies. Furthermore, these quasi-static flow pressures are the triangular hydrostatic pressure q_{hs} and the uniform hydrodynamic pressure q_{hd}. Considering $q_{hs} = \rho_w g h_w$, where ρ_w is the fluid density, and $q_{hd} = 0.5\rho_w C_p v_w^2$, where C_p is the pressure coefficient taken equal to 1.5 following the experiments of Jansen et al. (2020). The resulting trapezoidal diagram is described with the top pressure $q_{w,top} = q_{hd}$ and bottom pressure $q_{w,bot} = q_{hd} + q_{hs}$. Two common values of Fr lower than Fr_c are used, i.e. 0.6 and 1 following Petrone et al. (2017) to investigate two scenarios with different load severity. Taking h_w as the same as the impact point, i.e. $1.5m$, and considering the relationship between Fr, h_w and v_w mentioned above, $v_w = 2.3m/s$ and $3.84m/s$ for the two values of Fr, respectively. The impact velocity v_d is adapted to be equal to v_w [24,31,32]. Note that results are normalised with respect to v_d (see Eq. 6), allowing to directly compare F-t diagrams calculated under different v_d. This leads to two values of q_w: $q_{w,1,top} = 4.37kPa$ and $q_{w,1,bot} = 20.6kPa$, and $q_{w,2,top} = 12.2kPa$ and $q_{w,2,bot} = 28.3kPa$.

4. The boundary conditions (bc) are varied from the initial configuration of simply supported edges (bc #1 in Fig. A1). In one case, the base edge is fixed to obtain bc #4 (Fig. A1). In the other case, the top edge is made free to obtain bc #5 (Fig. A1). The value of δ is maintained by adapting the structure properties to the new boundary conditions.

To provide a global metric, the results are discussed in terms of θ_I, which is computed as:

$$\theta_I = \frac{I - I_{reference}}{I_{reference}} 100 \tag{7}$$

Where the impulse I is computed as [4]:

$$I = \int_0^{t_d} F(t)dt \tag{8}$$

2.3. The Mass and Stiffness Ratios Model (MSRM)

The Mass and Stiffness Ratios Model (MSRM) is the new model proposed in this research to compute the F-t diagrams of debris impacts on elastic structures integrating the effects of m_s for the scenarios of μ and δ belonging to D_{m_s}. The MSRM aims at replicating the characteristics of the numerical F-t diagrams calculated under the influence of the structural mass m_s, including the force spike (see Section 3.1). The output is a simplified nondimensional curve function of solely the structure-to-debris mass and stiffness ratios μ and δ that closely approximate the shape and the values of such numerical diagrams. The equations to compute such diagrams are formulated from general trends spotted for the main characteristics of the m_s-dependant F-t diagrams belonging to the dataset of numerical diagrams defined in Section 2.2.1 and presented in Section 3.1. The general validity of the data collected with the model presented in Section 2.2.1 allows to obtain generally valid MSRM outputs independent of the specific structural geometry and boundary conditions. The relative errors among the outputs of the MSRM equations and the numerical dataset are discussed.

The MSRM is finally compared with the ASCE model in realistic case studies to show the improvements introduced by the presented model with respect to the current design practice of ASCE/SEI 7–22. These analyses also allow to discuss the limits of the MSRM and to propose recommended models within the $\mu - \delta$ space. The reference results are obtained from solid debris impact models. Meanwhile, the MSRM and ASCE F-t diagrams are applied in equivalent impact force models, from which the structural displacements caused by these diagrams are extracted. The accuracy of the analytical models is assessed in terms of F-t diagrams and structural displacements. The case studies are defined from a database of realistic impact scenarios. These scenarios are defined for impacts on wall structures made of masonry, concrete and cross-laminated timber (referred to as XLAM hereafter but it is also known as CLT in the literature). These walls are defined with different realistic dimensions and mechanical properties taken from an extensive literature research. Boundary conditions are also varied based on common combinations of free, simply supported and fixed conditions of wall edges. These data are used to define such a broad set of realistic impact scenarios, whose full details are reported in Appendix A. Fig. 3 shows the entire set of 228 impact scenarios categorised based on their values of μ and δ. Among these, only the 169 cases belonging to D_{m_s} are selected to assess the MSRM.

3. Domain of importance of the structural mass

3.1. Critical mass and stiffness ratios

The critical mass and stiffness ratios μ_{cr} and δ_{cr} are obtained from the main dataset of numerical F-t diagrams computed with solid debris impact models. These F-t diagrams are shown in Fig. 4, where only some representative results are reported to avoid overcrowding. The numerical F-t diagrams are qualitatively compared with those calculated with the flex1DWP model, which is accurate when assuming $m_s = 0$ (see Section 2.2.1). For $\mu < 2$ and for every δ, the shape and values of the numerical F-t diagrams are compatible with that of the flex1DWP diagrams, conveying that m_s is not important for these values of μ and δ. Conversely, significant differences are observed for $\mu \geq 2$. Nevertheless, these differences depend on δ. For $\mu \geq 2$ and $\delta < 1$, the rigid-like F-t diagrams of the m_s-dependant results (see Section 1) are identified. These diagrams start with a spike that reaches $F_{nodim} \cong 1$ and have rectangular shapes with duration $t_{nodim} \cong 1$ and force values proportional to μ. These spikes are not associated with a strength spike in the material response as elastic materials are considered (see Section 2.1). It is worth noting that similar loading spikes are also observed for blast loads at the beginning of the loading phase [23,33]. The physical reasons behind these observed spikes are discussed in Section 3.3. In addition to [6], the present results also show proportionality between the force values and δ. Instead, for $\mu \geq 2$ and $1 < \delta < 5$, the F-t diagrams remain globally similar to the flex1DWP diagrams for μ immediately higher than 2, but an abrupt force rise and a notable reduction of the impact duration mark a substantial difference with respect to the massless solution. The rigid-like F-t diagrams are observed only for μ higher than $\cong 10$ and $1 < \delta < 5$. The peculiar behaviour of the cases having $1 < \delta < 5$ is expected since they are a separate category also under the massless structure assumption (see Section 1). These results convey that m_s is important for $\mu \geq 2$. However, the variability of the results progressively decreases as $\delta \rightarrow 5$, where they converge to the rigid1DWP diagrams, aligning with [6] which show that the effects of m_s are null for rigid impacts, i.e. $\delta > 5$. Therefore, m_s is important only if $\delta < 5$ also occurs.

A quantitative comparison between the numerical and flex1DWP F-t diagrams is provided using the error ε_{td} (see Section 2.2.1), whose values are shown in Fig. 5 as a function of μ and for different δ. These data show that, for $\mu < 2$, ε_{td} is within the ±5% band deemed as acceptable (see Section 2.2.1), while it is outside this band for $\mu \geq 2$, conveying that m_s is important for mass ratios $\mu \geq 2$. This trend is observed for every value

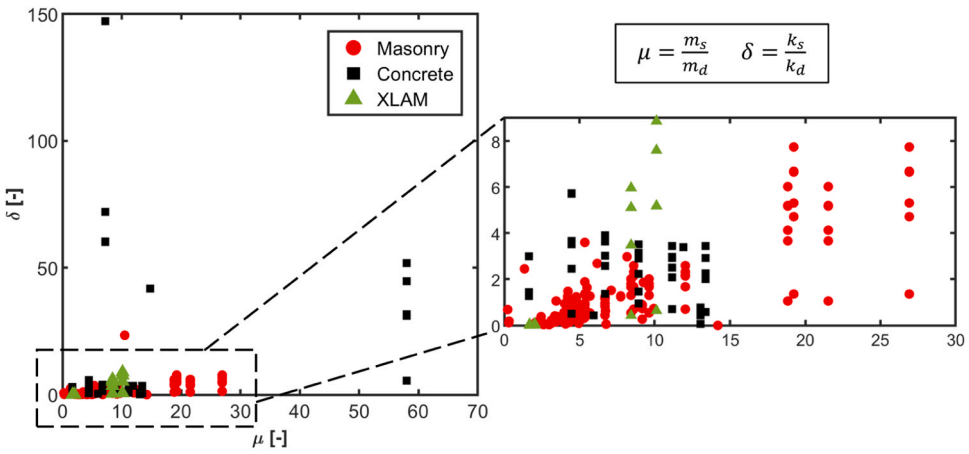

Fig. 3. Realistic impact scenarios in terms of μ and δ.

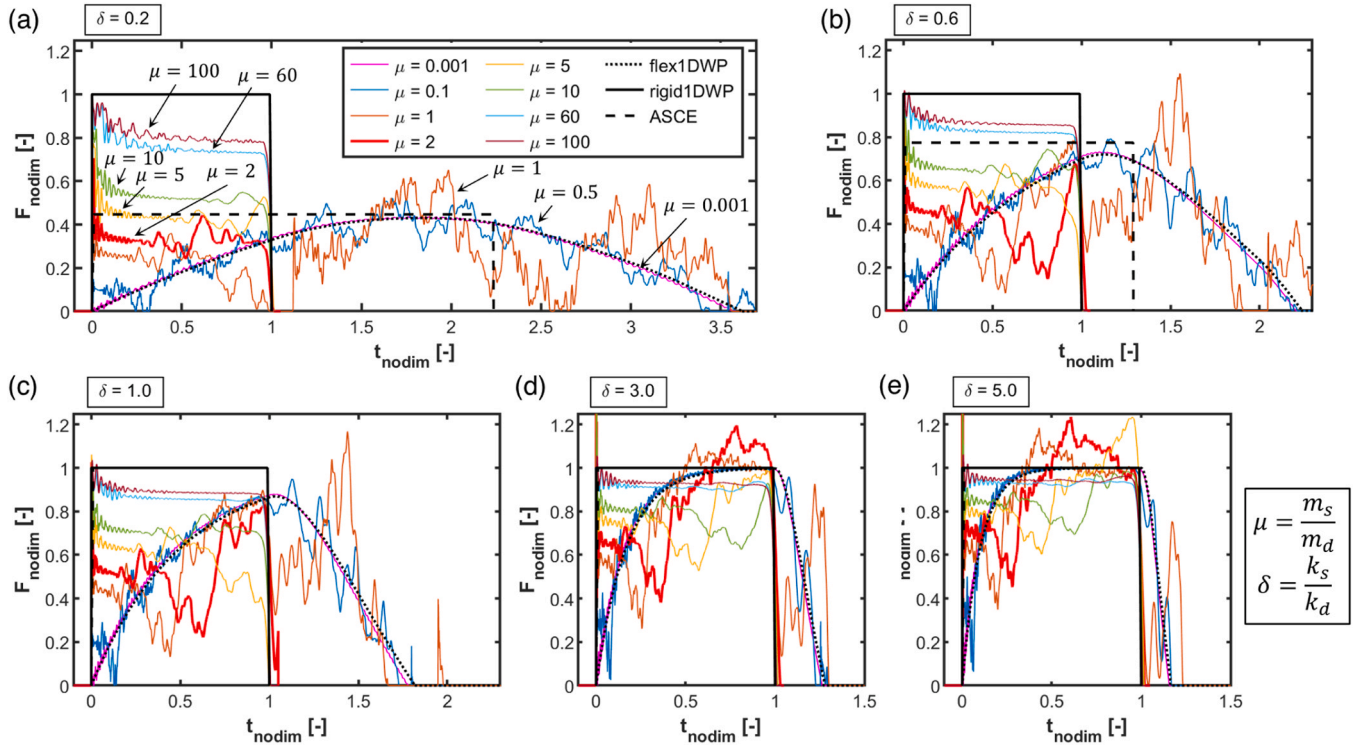

Fig. 4. F-t diagrams for various μ and (a) $\delta = 0.2$, (b) $\delta = 0.6$, (c) $\delta = 1$, (d) $\delta = 3$, (e) $\delta = 5$.

of stiffness ratio δ, but ε_{td} progressively decreases as $\delta \rightarrow 5$. Note that these ranges of μ and δ, and the related discussion, align with those individuated from the qualitative comparison discussed in the previous paragraph.

Therefore, considering the presented qualitative and quantitative comparisons, m_s is important in a domain D_{m_s} such that μ is higher than a critical $\mu_{cr} = 2$ and δ is lower than a critical $\delta_{cr} = 5$. Moreover, to consider the characteristics of the cases having $1 < \delta < 5$ and $2 < \mu < 10$, D_{m_s} is split into two complementary subdomains, $D_{m_s,1}$ for the general cases and $D_{m_s,2}$ for such cases. These domains are shown in Fig. 6, where realistic impact scenarios are also reported, pointing out that many of realistic scenarios belong to both subdomains (see Fig. 6). Thus, a correct prediction of the F-t diagrams in both domains is important for practical applications. As an example, some of these realistic impact scenarios that belong to D_{m_s} are highlighted in Fig. 6. These scenarios have a log debris compatible with the minimum design demand imposed by ASCE and the following structures:

- Scenario 1: the SB01 clay masonry wall tested by Chong (1993), which is 5.615m wide, 2.475m tall and 0.1025m thick. Boundary conditions are clamped base, simply supported vertical edges and free top edge. This wall can be represented with homogeneous properties using density equal to 1680kg/m^3 and Youngs' modulus equal to 14000MPa [19]. Here, $\mu = 5.3$ and $\delta = 0.25$.
- Scenario 2: a calcium silicate masonry wall typical of Dutch residential buildings analysed by Jansen et al. (2020), which is 8.64m wide, 2.7m tall and 0.1m thick. Boundary conditions are clamped base and vertical edges and simply supported top edge. This wall can be represented with homogeneous properties using density equal to 1800kg/m^3 and Youngs' modulus equal to 14000MPa. Here, $\mu = 10.5$ and $\delta = 0.71$.

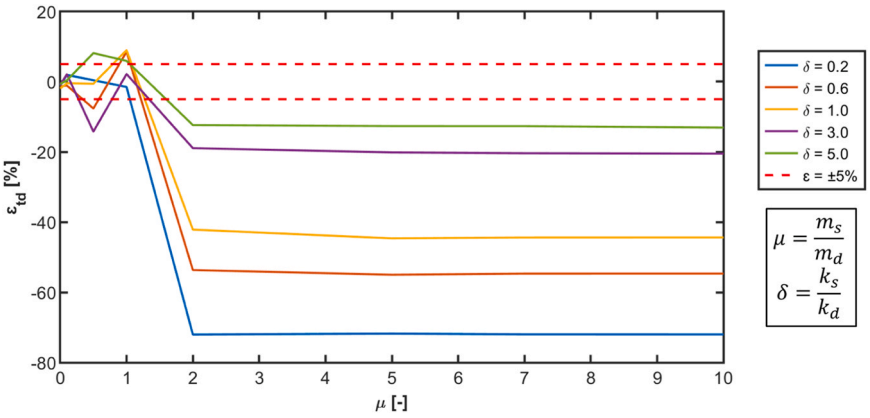

Fig. 5. Values of ε_{td} for different μ.

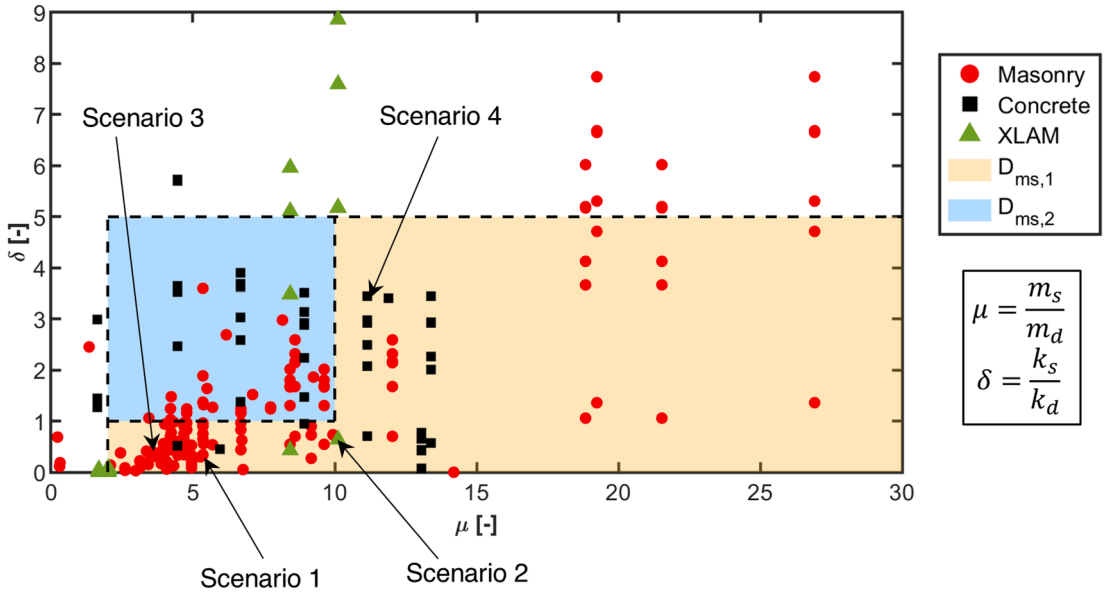

Fig. 6. D_{m_s} within the $\mu - \delta$ space and superimposition with realistic debris impact scenarios.

- Scenario 3: the concrete masonry infill analysed by Dawe and Seah [5], which is 3.6m wide, 2.8m tall and 0.14m thick. Boundary conditions are simply supported at all edges. This wall can be represented with homogeneous properties using density equal to 1363kg/m^3 and Youngs' modulus equal to 17500MPa. Here, $\mu = 4.24$ and $\delta = 0.77$.
- Scenario 4: a typical concrete wall (dimensions.com) [9], which is 5m wide, 2.7m tall and 0.15m thick. Boundary conditions are clamped at all edges. This wall can be represented with homogeneous properties using density equal to 2500kg/m^3 and Youngs' modulus equal to 30000MPa. Here, $\mu = 11.2$ and $\delta = 3.5$.

The presented data also allow discussing their potential adaptation to other debris types like cars or shipping containers. The crucial role of the mass and stiffness ratio conveys that other debris types might be studied with a similar methodology and lead to similar findings in terms of critical ratios δ_{cr} and μ_{cr}. However, the main limitation is that other debris types have different geometries than a log, e.g. larger dimensions or crushing zones in case of cars, which requires specific analyses that represent these geometries accurately. Investigating the impact of these debris is out of the scope of this study, but we aim to examine them in detail in future studies. Finally note that the crucial role of structural stiffness in defining the F-t diagrams suggests that structural damage may affect the impact force through its degrading effect on the structural stiffness. The investigation of this topic is of interest given the evidence of structural damage occurring in extreme hydrodynamic events due to debris actions, also as repeated impacts (see Section 1). However, specific analyses are required, which will be carried out in future studies.

3.2. Influence of vertical and horizontal loads and boundary conditions

The influence of SW, p, q_w and bc on D_{m_s} are investigated using representative values of μ and δ in $D_{m_s,1}$ and $D_{m_s,2}$. For SW, the cases investigated in $D_{m_s,1}$ are $\delta = 0.4$ with $\mu = 0.1$, 2, 5, 20, 40, and 100, and $\delta = 1$, 3 and 5 with $\mu = 20$. In $D_{m_s,2}$, they are $\delta = 1$, 3 and 5 with $\mu = 2$. For p, q_w and bc, the cases investigated in $D_{m_s,1}$ are $\delta = 0.4$ with $\mu = 20$. In $D_{m_s,2}$, they are $\delta = 3$ with $\mu = 2$. The results analysing SW (Fig. 7-a), p (Fig. 7-b) and q_w (Fig. 7-c) show that these loads do not modify the F-t diagrams since they do not differ from those with no SW, no p and no q_w, respectively. Only some representative curves are reported for the SW analyses for a better data presentation. The values of θ_I (see Eq. 7) are minimal. For SW, the average of their absolute values is equal to 0.02 % and the standard deviation to 0.01 %. For p, the average of their absolute values is equal to 0.06 % and the standard deviation to 0.03 %. For q_w, the average of their absolute values is equal to 0.7 % and the standard deviation to 0.6 %. Detailed values are reported in Appendix D. These

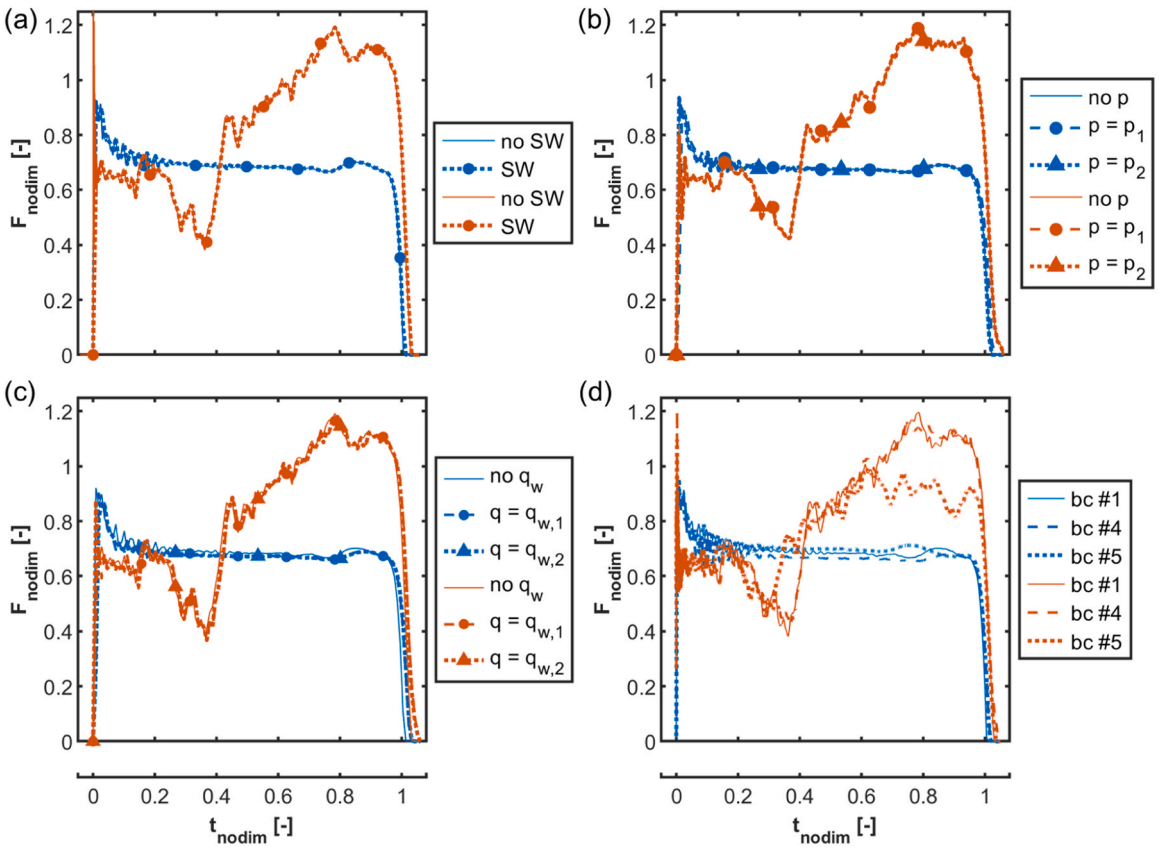

Fig. 7. (a) SW, (b) p, (c) q_w and (d) bc for $\delta = 0.4$ and $\mu = 20$ (blue) and $\delta = 3$ and $\mu = 2$ (orange).

data convey that SW, p and q_w do not influence D_{m_s}.

Conversely, the results analysing bc (Fig. 7-b) indicate that they moderately affect the F-t diagrams. When $\delta = 0.4$ and $\mu = 20$, the plateau force varies. When $\delta = 3$ and $\mu = 2$ with bc #5 with, the peak force decreases. The values of θ_I are -2.38% and 1.49% for bc #4 and bc #5, respectively, if $\delta = 0.4$ and $\mu = 20$, and -0.04% and -6.1% for bc #4 and bc #5, respectively, if $\delta = 3$ and $\mu = 2$. However, the shape of the F-t diagrams is unvaried, indicating that bc do not influence D_{m_s}.

3.3. Physical explanation of the results

The results for $\delta = 0.4$ and $\mu = 0.001$ (Fig. 8-a) and $\mu = 20$ (Fig. 8-b) are presented as representative examples. The curves F_m and $(R_{TOT} + F_m)$ are plotted with opposite sign to support the discussion. When $\mu = 0.001$, F_m is close to zero, which is expected given the low value of m_s in this case. As such, F_m can be neglected and the dynamic equilibrium (Eq. 3) is satisfied by F and R_{TOT} only, which have the similar, but opposite in sign, time histories (see Fig. 8-a). Conversely, when $\mu = 20$, F_m is not negligible given the much higher value of m_s and actively participate into the dynamic equilibrium (see Fig. 8-b). The sharp rise in the impact

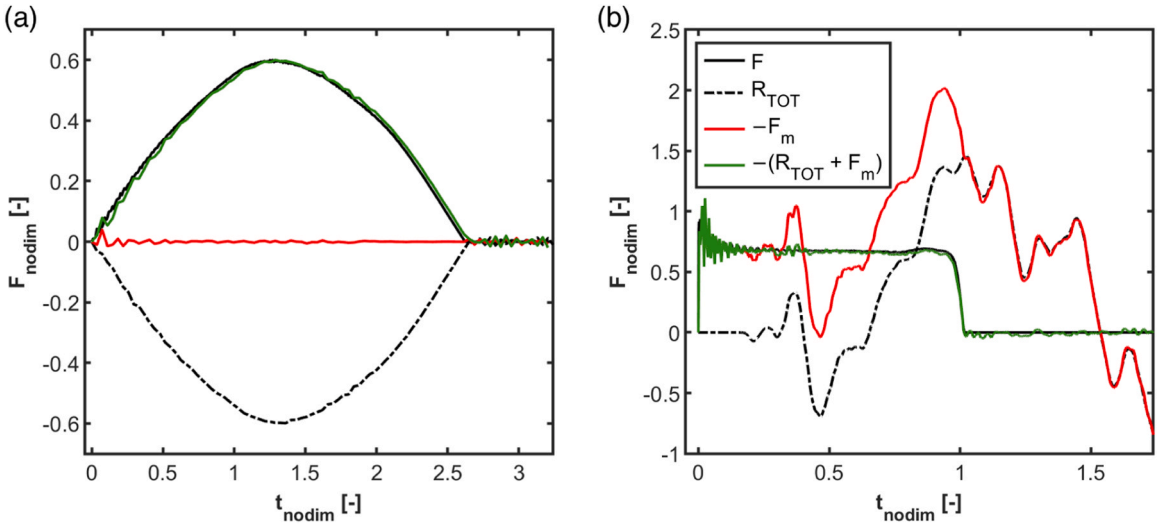

Fig. 8. Time histories of F, R_{TOT} and F_m for $\delta = 0.4$ and (a) $\mu = 0.001$ and (b) $\mu = 20$.

force is initially balanced by F_m. Subsequently, F_m and R_{TOT} have an almost constant sum, causing the plateau of the impact force. Therefore, the F-t diagram of the m_s-dependant impacts is caused by the combined resistance opposed by the structural stiffness and inertia forces.

It is also worth noting that R_{TOT} in Fig. 8-b lags with respect to F. This is explained considering the elastic stress waves propagation in the structure at speed c (Fig. 9-a). Such a propagation cause R_{TOT} to arise only when the stress waves reach the supported perimeter. This is further demonstrated by the reaction forces R_1, R_2 and R_3 on three equal segments along half of the top edge (Fig. 9 - a). Their arising time is compatible with t_1, t_2 and t_3 (Fig. 9 - d), which are the times needed for a stress wave to reach the related segments from the impact zone, i.e. equal to the travel distance divided by c. Conversely, R_{TOT} does not lag if $\mu = 0.001$ because the low m_s, associated to low ρ_s, makes c significantly higher than the case having $\mu = 20$. As such, stress waves propagates faster and no significant lags are observed for R_{TOT} (Fig. 8-a).

A correlation between c and the structural displacements is also found. The displacements u_1 and u_2 are measured as indicated in Fig. 9 - b and plot in Fig. 9 - e. The time t_p is the time needed for stress waves to travel across the structure thickness and equal to $t_p = b_s/c$. Between $t = 0$ and $t = t_p$, u_1 is greater than zero but u_2 is null since the waves have not reached yet its control point. The displacement u_2 starts at t_p. Additionally, global displacements at significant time points (Fig. 10-a) are reported for the impact and back faces (Fig. 10-b). The structure is effectively undeformed until t_p, with only minor displacements at the impact point, in line with Fig. 9 - e. Major displacements occur after t_p. Data in Fig. 9 and Fig. 10 are a consequence of m_s. Increasing the structural mass m_s means increasing the structure density ρ_s, slowing down the stress waves speed c (see Eq. 4). Therefore, since the structure does not deform instantly as a whole, but each part displaces progressively as elastic waves reach it, the decreased c due to ρ_s causes a slower structural response as m_s increases. Thus, at the beginning of impact, the plate-type structure effectively behaves as a rigid body, showing only a limited local deformation at the impact location (see Fig. 9-e and Fig. 10-c). This causes an abrupt rise of impact force, which is typical of rigid impacts [26]. Out-of-plane plate deformations occur only after stress waves reach the back face of the wall, i.e. after t_p (see Fig. 9-e and Fig. 10-c), conveying that the structure does not behave as a rigid body anymore but is now flexible and bends under the impact action. This bending causes a decrease in the impact force after t_p (see Fig. 9-e). Therefore, the spike observed in the F-t diagrams (see Section 3.1) is determined by the transition from rigid to flexible structural response. Note that the spike nondimensional force is close to 1, which is consistent with the initial rigid structural response as $F_{nodim} = 1$ is the value of the peak force of rigid impacts (see Appendix A). After the spike occurs, stress waves continue propagating throughout the structure and major out-of-plane deformation occurs in the plate (see t_3 in Fig. 9-c). Here, the plate responds with its structural stiffness k_s function of the structural

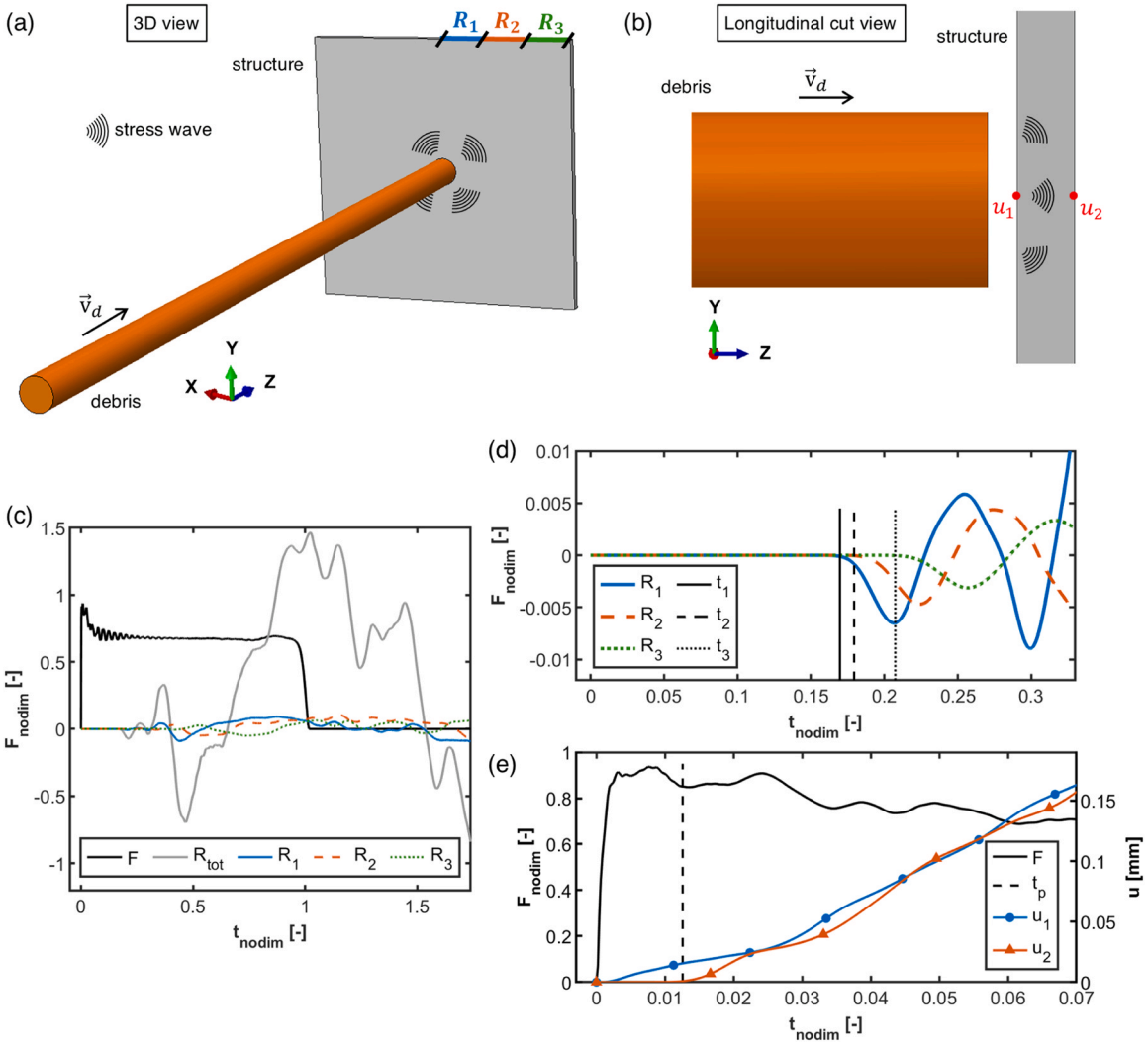

Fig. 9. Stress wave propagation in the structure (a) globally and (b) across the thickness. (c) comparison of F and R_{TOT}, (d) time-zooming of R_1, R_2 and R_3. (e) time-zooming of u_1 and u_2.

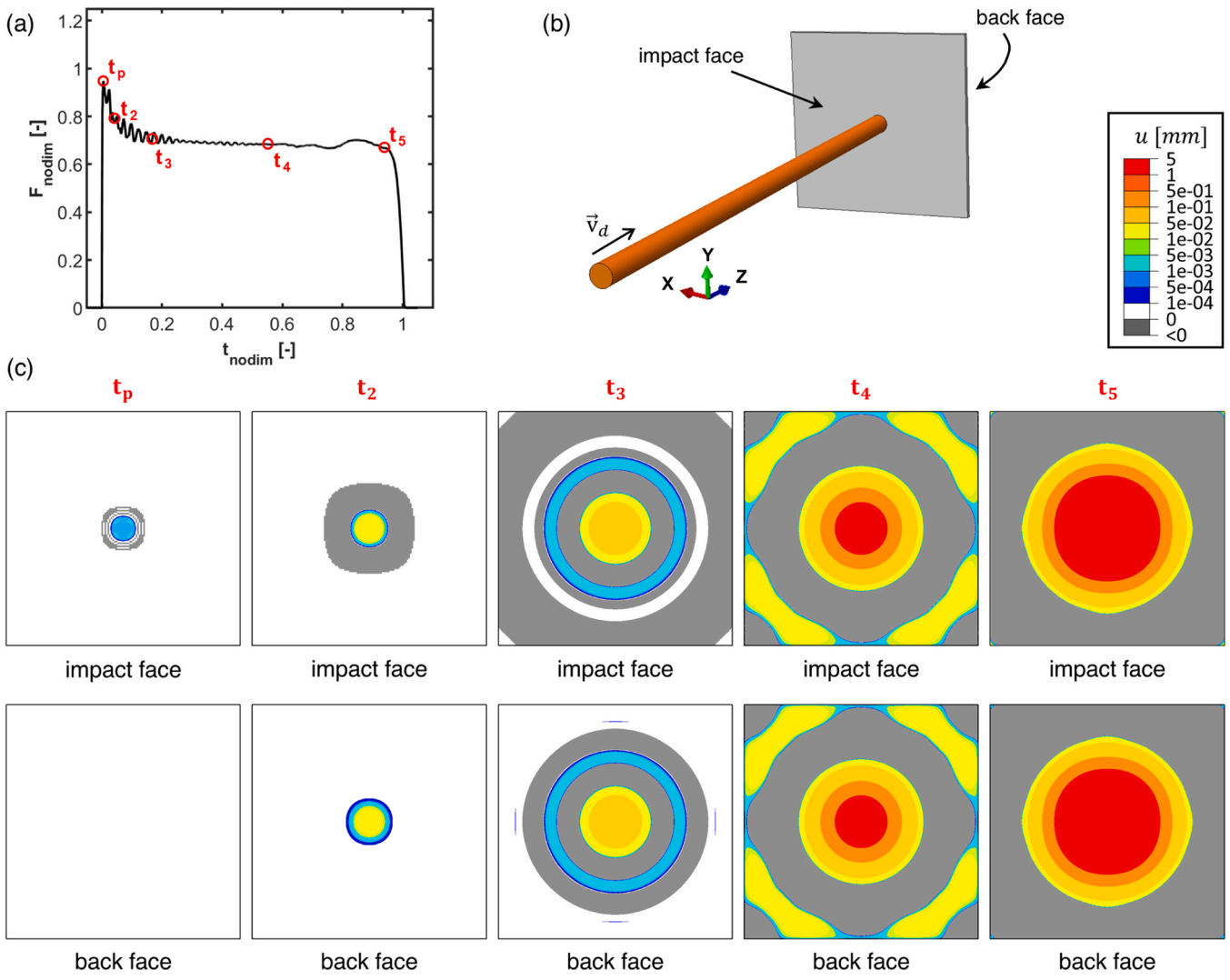

Fig. 10. (a) Significative time points, (b) impact and back faces and (c) displacement contours.

bending behaviour (see Section 2.2.1). The plateau force observed after this point is caused by the equilibrium between impact action and structural response in terms of elastic and inertia reactions (see Fig. 8-b and related discussions). Note that the physical explanation provided for the impact force spike aligns with blast load scenarios, where the initial load spike is caused by the reflection of the pressure wave front that

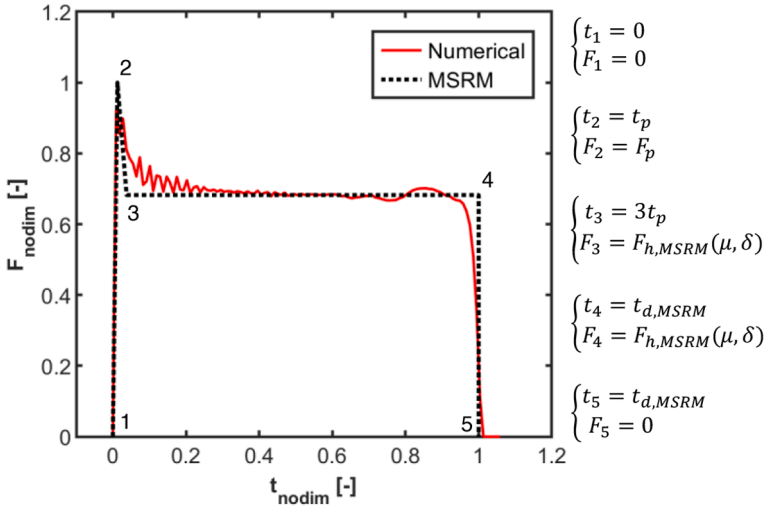

Fig. 11. Numerical and MSRM F-t diagrams.

reflects on the hit structure at the beginning of the loading phase.

4. The Mass and Stiffness Ratios Model (MSRM)

4.1. The MSRM F-t diagrams

The F-t diagrams of the MSRM (Fig. 11) are a multilinear simplified representation of the m_s-dependent F-t diagrams (Fig. 4). The MSRM diagrams are tailored to represent the numerical F-t diagrams calculated under the influence of m_s and presented in Section 3.1. The characteristic shape of the cases belonging to $D_{m_s,1}$ is considered (see Fig. 4), but this is adapted also for those of $D_{m_s,2}$ as specified in the next paragraph.

The values of t_p and F_p, i.e. the spike main parameters, are set following Section 3.3, with $F_p = 1$ being an accurate approximation. The spike end time t_3 is equal to $3t_p$ observing its accuracy in replicating the data of Fig. 4. Moreover, $t_{d,MSRM} = 1$, which is the nondimensional duration of rigid impacts (see Appendix A) and represents well the rigid-like impacts caused by m_s (see Fig. 4). Finally, $F_{h,MSRM}(\mu, \delta)$, i.e. the plateau main parameter, is evaluated from $F_{h,r}$, which are the plateau forces of the F-t diagram in Fig. 4 for the r-th pair (μ_i,δ_j). In $D_{m_s,1}$, $F_{h,r}$ is the average force between $t = 0.3t_d$ and $t = 0.8t_d$ to be sufficiently far from the plateau extremes and capture its overall trend. In $D_{m_s,2}$, $F_{h,r}$ is the adapted as the value to which the F-t diagram converges after the spike. An exponential relation is observed between μ and $F_{h,r}$ for fixed values of δ (Fig. 12-a) and fit with the equation:

$$F_{h,MSRM}(\mu, \delta) = A_{1,\delta}\exp(A_{2,\delta}\mu) + A_{3,\delta}\exp(A_{4,\delta}\mu) \tag{9}$$

with $A_{1,2,3,4,\delta}$ defining the fitting curves (see Table 1), which are shown in Fig. 12-a.

The accuracy of the MSRM F-t diagrams is assessed with respect to the data of Fig. 4 for $t_{d,MSRM}$ and $F_{h,MSRM}$. The impulse I (see Eq. 8) is also evaluated to provide a global accuracy estimation. The errors ε_{td}, ε_{Fh} and ε_I are computed for each r-th pair of μ_i and δ_i as:

$$\varepsilon_{td}(\mu_i, \delta_j) = \frac{t_{d,MSRM,r} - t_{d,r}}{t_{d,r}} 100 \tag{10}$$

$$\varepsilon_{Fh}(\mu_i,\ \delta_j) = \frac{F_{h,MSRM,r} - F_{h,r}}{F_{h,r}} 100 \tag{11}$$

$$\varepsilon_I(\mu_i, \delta_j) = \frac{I_{MSRM,r} - I_r}{I_r} 100 \tag{12}$$

The values of ε_{Fh}, ε_{td} and ε_I are shown in Fig. 12-b to d, indicating that they are mostly included within a ±5% error band. Only ε_I exceeds the 5% threshold for $2 < \mu < 10$. Among these, those having $1 < \delta < 5$, i.e. that belong to $D_{m_s,2}$ have ≅ 20% negative errors, which is expected given the peculiarities of these cases and their adaptation to the MSRM. Instead, those having $\delta < 1$ have ≅ 15% positive errors likely due to the oscillations of the numerical diagram. However, the generally low errors validate the MSRM equations. It is worth noting that using the recorded values of F_p instead of $F_p = 1$ does not affect the results. The error ε_I varies of ≅ 1 %, which is expected given that t_p is one order lower than t_d (see Section 3.3), making the spike duration a small part of the total impact duration and its contribution to I minimal. Also, neither ε_{Fh} and ε_{td} are affected by F_p.

4.2. Analysis of realistic case studies

The MSRM and ASCE models are applied in the realistic case studies described in Section 2.3, aiming to assess the accuracy of the MSRM in relation to that of the ASCE model. The comparison is made in terms of the errors ε, defined in Eqs. 13–16, in calculating t_d, F_h and I and the maximum structural displacement u_{max} caused by the considered F-t diagrams. The following errors are computed:

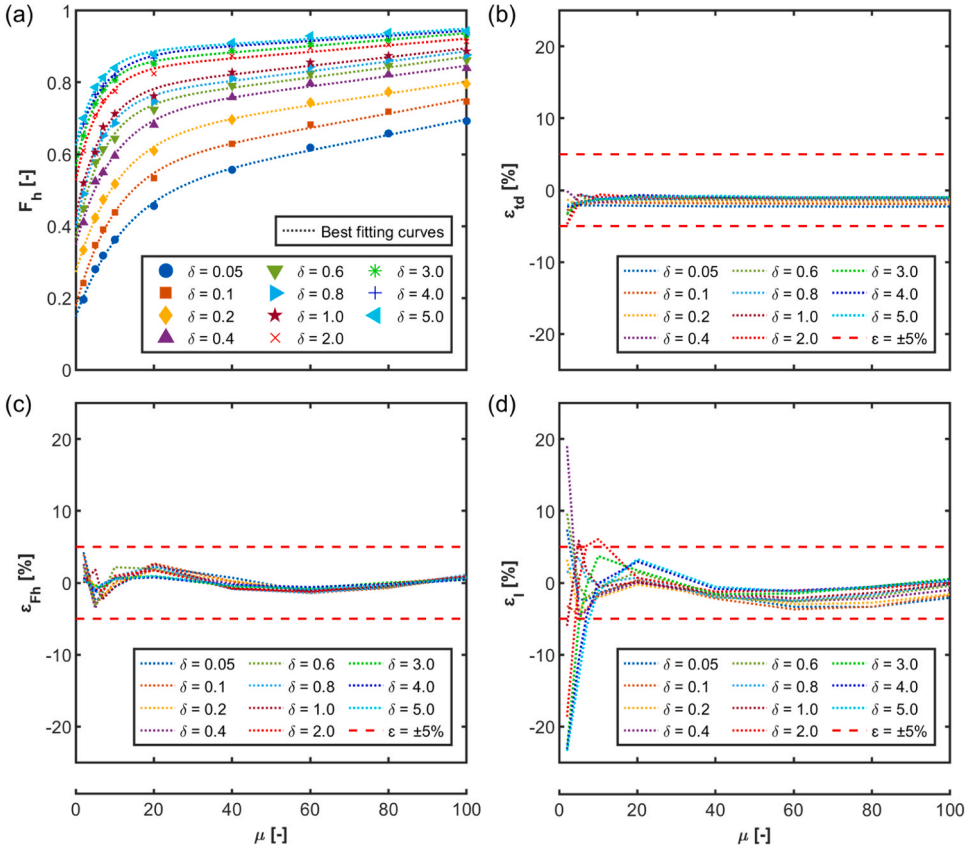

Fig. 12. Values of (a) $F_{h,r}$ and $F_{h,MSRM}$ curves, (b) ε_{td}, (c) ε_{Fh} and (d) ε_I.

Table 1
Coefficients $A_{1,2,3,4,\delta}$ of Eq. 9. Intermediate values can be linearly interpolated.

δ [−]	$A_{1,\delta}$ [−]	$A_{2,\delta}$ [−]	$A_{3,\delta}$ [−]	$A_{4,\delta}$ [−]	δ [−]	$A_{1,\delta}$ [−]	$A_{2,\delta}$ [−]	$A_{3,\delta}$ [−]	$A_{4,\delta}$ [−]
0.05	0.50720	0.00319	− 0.35905	− 0.07862	1	0.77827	0.00140	− 0.34964	− 0.14711
0.1	0.57024	0.00280	− 0.39335	− 0.09784	2	0.83243	0.00102	− 0.30545	− 0.16544
0.2	0.65075	0.00209	− 0.37918	− 0.09407	3	0.84962	0.00098	− 0.28199	− 0.17952
0.4	0.71141	0.00174	− 0.36325	− 0.10726	4	0.87452	0.00077	− 0.25013	− 0.14575
0.6	0.73423	0.00171	− 0.36671	− 0.14125	5	0.88006	0.00076	− 0.25585	− 0.18054
0.8	0.75450	0.00161	− 0.35883	− 0.15837					

$$\varepsilon_{td,MSRM} = \frac{t_{d,MSRM} - t_{d,cs}}{t_{d,cs}} 100, \quad \varepsilon_{td,ASCE} = \frac{t_{d,ASCE} - t_{d,cs}}{t_{d,cs}} 100 \tag{13}$$

$$\varepsilon_{Fh,MSRM} = \frac{F_{h,MSRM} - F_{h,cs}}{F_{h,cs}} 100, \quad \varepsilon_{Fh,ASCE} = \frac{F_{h,ASCE} - F_{h,cs}}{F_{h,cs}} 100 \tag{14}$$

$$\varepsilon_{I,MSRM} = \frac{I_{MSRM} - I_{cs}}{I_{cs}} 100, \quad \varepsilon_{I,ASCE} = \frac{I_{ASCE} - I_{cs}}{I_{cs}} 100 \tag{15}$$

$$\varepsilon_{u,MSRM} = \frac{u_{\max,MSRM} - u_{\max,cs}}{u_{\max,cs}} 100, \quad \varepsilon_{u,ASCE} = \frac{u_{\max,ASCE} - u_{\max,cs}}{u_{\max,cs}} 100 \tag{16}$$

where the subscript "cs" indicates the numerical case study results. The errors are presented with contour plots with thresholds − 30%, − 20%, − 10%, − 5%, 0%, 5%, 10%, 20%, 60% and 120%, selected to distinguish between positive and negative errors and to optimise data presentation. The frequency of the errors is also presented using histograms.

The errors ε for the impact duration, plateau force, impulse and maximum structural displacement, t_d, F_h, I and $u_{\max}$, respectively, are reported in Fig. 13, where each case study is represented with a point with coordinates of the mass and stiffness ratios μ and δ, respectively. Data show that the ASCE model generally overestimates t_d, F_h, I and $u_{\max}$ with errors highly concentrated in the frequency bands between 20% and 120%, except for $\varepsilon_{td,ASCE}$ in cases with $\delta > 1$, for which $-5\% < \varepsilon_{td,ASCE} < 0$. It is worth noting that $\varepsilon_{Fh,ASCE}$, $\varepsilon_{I,ASCE}$ and $\varepsilon_{u,ASCE}$ decrease as δ increases, which is expected since the numerical F-t diagrams tend to the rigid impact solution for $\delta \to 5$ (see Section 3.1). The significant inaccuracies of the ASCE model are shown also in Fig. 4, given the substantial differences with the numerical diagrams.

Conversely, the MSRM is significantly more accurate than the ASCE model. This is conveyed by the error frequencies mostly concentrated in the bands between −10% and +10% (see Fig. 13). In particular, the frequency distribution of $\varepsilon_{u,MSRM}$ (Fig. 13-n) is as follows: the 47 % of the cases are associated with $-5\% < \varepsilon_{u,MSRM} < 5\%$, the 26 % with $-10\% < \varepsilon_{u,MSRM} < -5\%$ and the 5% with $5\% < \varepsilon_{u,MSRM} < 10\%$. The other 22 % has non-negligible errors: $\varepsilon_{u,MSRM} < -20\%$ (the 3.5 %), $-20 < \varepsilon_{u,MSRM} < -10\%$ (the 9.5 %), $10\% < \varepsilon_{u,MSRM} < 20\%$ (the 6 %) and $\varepsilon_{u,MSRM} > 10\%$ (the 3 %). The errors distributions of $\varepsilon_{Fh,MSRM}$ (Fig. 13-f) and $\varepsilon_{I,MSR}$ (Fig. 13-i) are similar to $\varepsilon_{u,MSRM}$. Instead, $\varepsilon_{td,MSRM}$ is always between −5% and 0% (Fig. 13-c), which is expected given the consistency of the impact durations of the cases belonging to D_{m_s} (see Fig. 4). Fig. 14-a and b show a representative case study accurately predicted by the MSRM and mispredicted by the ASCE model.

The identified sources of the non-negligible errors of the MSRM are secondary impacts, the misprediction of F_h and the misprediction of the diagram shape in $D_{m_s,2}$. Regarding secondary impacts, the cases that present errors due to this source are those with significant impact force for $t_{nodim} > 1$ (see a representative example in Fig. 14-c). Here, the displacements of the MSRM are accurate until $t_{d,MSRM}$, and underestimated after it as the MRSM diagram ends at $t_{nodim} = 1$ (see Fig. 14-d). The results of the ASCE model are also reported. In line with Fig. 13, they significantly overestimate the response. All cases with $\varepsilon_{u,MSRM} < -20\%$ experience secondary impacts, conveying a correlation between them. Another correlation is observed with the values of μ since 68 % of cases having secondary impacts have μ immediately higher than 2. Therefore, it is possible that these are boundary cases where the effects of m_s are sufficiently high to cause a rigid-like structural behaviour, but not enough to bounce the debris back, which the continues to interact with the structure. However, these secondary impacts might not occur in a realistic hydrodynamic scenario as the log likely rotates and changes direction after the first impact as driven by the flow. The current model cannot replicate such behaviour since the water flow is not modelled, and specific experimental or numerical studies are needed to understand secondary impacts. The exclusion of the fluid phase in the model also leads to not consider the effects of the surrounding water between the debris and the structure. However, despite influencing the F-t diagrams, these effects are expected to be limited for log debris as these have small cross-section areas (see Section 2.1). Nevertheless, future dedicated studies are needed to assess how the effects of such surrounding water interact with the m_s effects, particularly for debris with larger cross-sections like shipping containers or cars.

Excluding the cases with errors from secondary impacts and the misprediction of the F-t diagram shape in $D_{m_s,2}$ (discussed in the next paragraph), the F_h misprediction leads to all the errors $\varepsilon_{u,MSRM} < -5\%$ if $\varepsilon_{Fh,MSRM} < 0$ and $\varepsilon_{u,MSRM} > +5\%$ if $\varepsilon_{Fh,MSRM} > 0$. In general, $|\varepsilon_{u,MSRM}|$ is proportional to $|\varepsilon_{Fh,MSRM}|$. See a representative example in Fig. 14-e, f, where the results of the ASCE model are also reported. In line with Fig. 13, they significantly overestimate the response. Among these cases, some boundary conditions are more frequent than in the whole database. When $\varepsilon_{u,MSRM} < -5\%$, these are bc #5, #8 and #9 (Fig. A1), which are among those that give the lowest k_s with the same geometrical and mechanical parameters. When $\varepsilon_{u,MSRM} > 5\%$, these are bc #2, #3, #4 and #10 (Fig. 1B), which are among those that give the highest k_s. These data aligns with Fig. 7-d.

Regarding the misprediction of the F-t diagram shape in $D_{m_s,2}$, these errors are expected given the adaptation of the MSRM in this subdomain (see Section 4.1). A representative case study is in Fig. 14-g, h. The results of the ASCE model are also reported. In line with Fig. 13, they significantly overestimate the response. The results of the flex1DWP are also reported and discussed, considering the similarity between the numerical and flex1DWP F-t diagrams in these scenarios (see Section 3.1). The error $\varepsilon_{u,flex1DWP}$ is computed consistently with Eq. 16. In Fig. 14-h, $\varepsilon_{u,MSRM}$ is negative since the MSRM underestimates the force after $t_{nodim} = 0.5$. Conversely, ASCE and the 1DWP models overestimate the response, with $\varepsilon_{u,flex1DWP} < \varepsilon_{u,ASCE}$ since it better approximate the shape of the numerical F-t diagram. Fig. 15 gives an overview of the case studies in $D_{m_s,2}$, confirming the errors hierarchy $\varepsilon_{u,MSRM} < 0 < \varepsilon_{u,flex1DWP} < \varepsilon_{u,ASCE}$.

4.3. Recommended models in the $\mu - \delta$ space

It is finally pointed out which are the recommended models to use to compute the F-t diagrams of log debris impacts on structures across the $\mu - \delta$ space (Fig. 16). Following Sections 4.1 and 4.2, the MSRM is recommended in $D_{m_s,1}$ given its general accuracy. Instead, the flex1DWP is preferable in $D_{m_s,2}$ since it generally captures the shape of the numerical F-t diagrams, but the ASCE model is a possible alternative. Outside D_{m_s}, the F-t diagrams are correctly predicted by the flex1DWP for $\mu < 2$ and $\delta < 5$, as shown in Fig. 4, making such a model preferable in this range. Finally, for $\delta > 5$, the impact is rigid and accurately represented by the

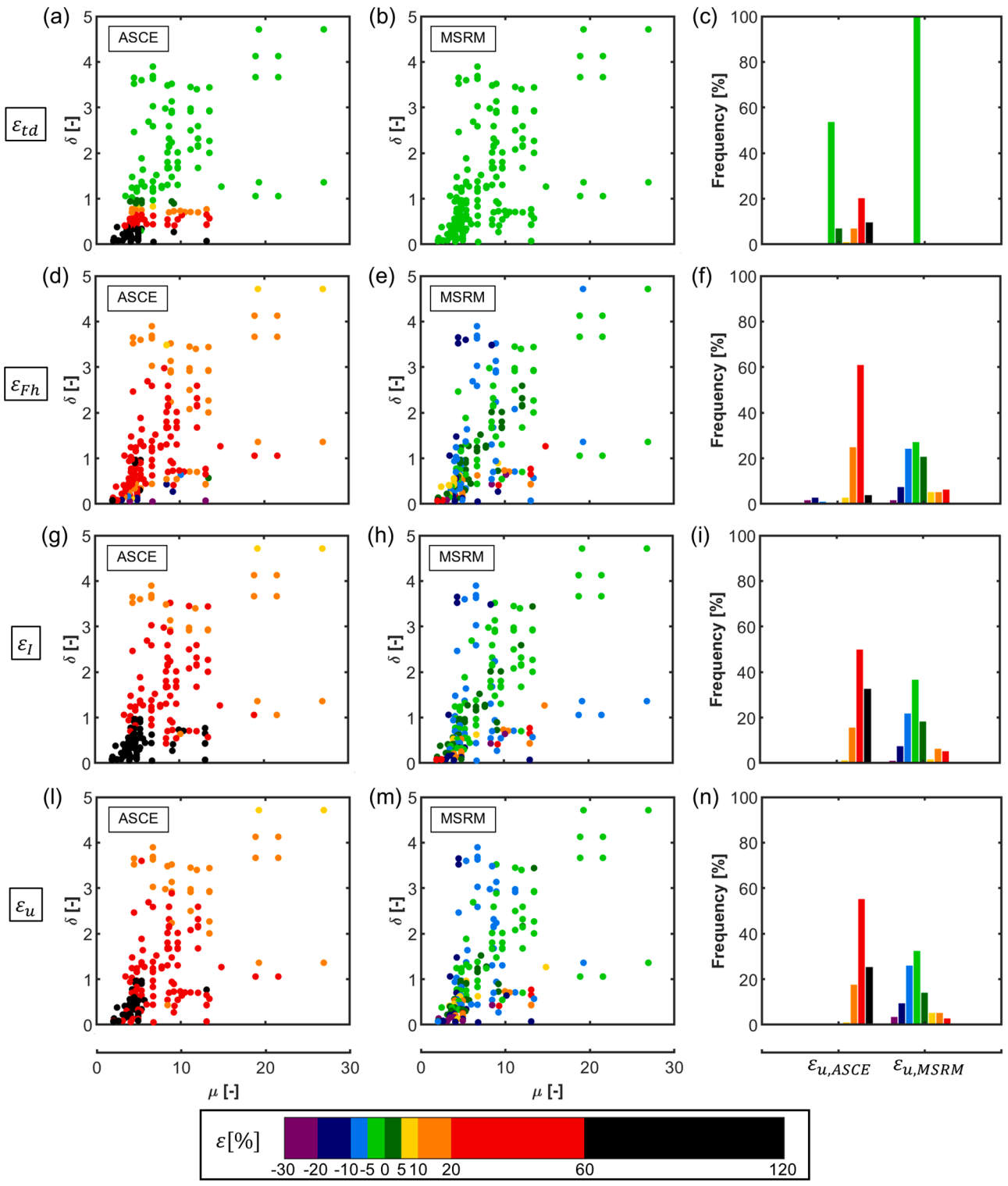

Fig. 13. Errors ε when using ASCE and MSRM models in case studies and their relative frequencies: (a, b, c) ε_{td}, (d, e, d) ε_{Fh}, (g, h, i) ε_I and (l, m, n) ε_{umax}.

rigid1DWP and ASCE models, which coincide in this range (see Appendix A). The case studies are also plotted in Fig. 16 as a reference.

5. Conclusions

The objectives of this study were to define the domain D_{m_s} in the design space of structure-to-debris mass and stiffness ratios, μ and δ, respectively, in which the structural mass m_s is important, and to propose a new analytical model, the Mass and Stiffness Ratios model (MSRM), to accurately compute the F-t diagrams in this domain. Finite Elements (FE) dynamic simulations were carried out to simulate the impact scenarios. To investigate a broad range of μ and δ, we used a square plate structure with varying properties and fixed debris compatible with the minimum design demand given by ASCE/SEI 7–22. The MSRM and the ASCE model by ASCE/SEI 7–22 were finally applied in realistic case studies and their results were compared.

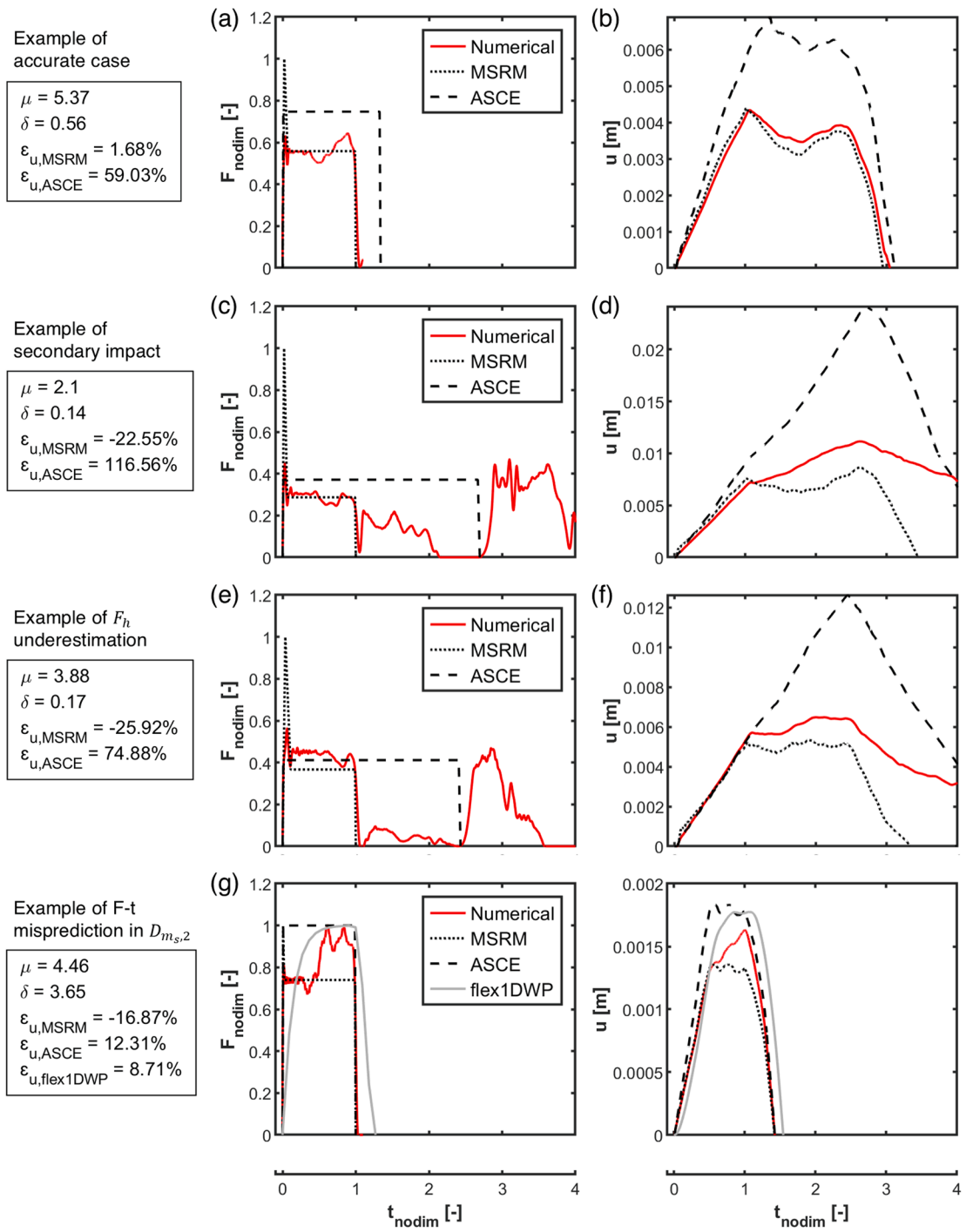

Fig. 14. Representative case studies for (a,b) accurate cases, (c,d) error due to secondary impacts, (e,f) error due to F_h underestimation and (g,h) misprediction of the F-t diagram shape within $D_{m_s,2}$.

The main findings were:

1. The D_{m_s} was found in a region with μ greater than a critical value $\mu_{cr} = 2$ and δ lower than a critical value $\delta_{cr} = 5$. Moreover, D_{m_s} was found independent from structural self-weight, vertical and horizontal external loads and structural boundary conditions. The domain D_{m_s} includes several realistic impact scenarios on structures like a masonry wall being $8.64m$ wide, $2.7m$ tall and $0.1m$ taken from typical Dutch residential buildings or a common concrete wall being $5m$ wide, $2.7m$ tall and $0.15m$ thick.
2. We proposed, for the first time, an analytical model, the MSRM model, that computes the F-t diagrams of log debris impacts on structures integrating the effects of m_s and provides highly accurate results. This accuracy was shown in terms of F-t diagrams and caused structural displacements. The MSRM fill the gap identified by [6] about the lack of accurate analytical models to compute these F-t when m_s has crucial effects.
3. The F-t diagrams of the MSRM were defined as multilinear simplified curves. The equations to compute them were formulated from the general trends of the key parameters defining the F-t diagrams belonging to D_{m_s} and are a function of μ and δ only.

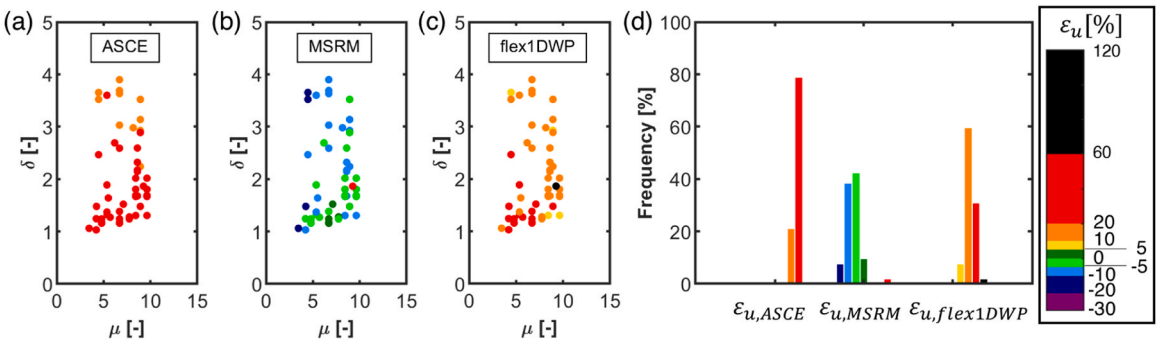

Fig. 15. ε_u for case studies in $D_{m_s,2}$ using (a) ASCE, (b) MSRM and (c) flex1DWP models, and (d) their frequency distribution.

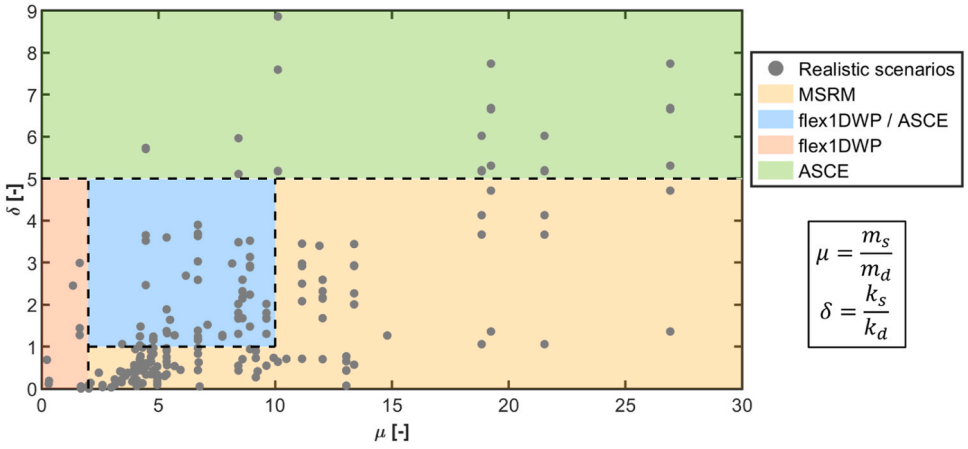

Fig. 16. Most accurate models in the $\mu - \delta$ space.

4. The MSRM improved upon the significantly overestimating results of the ASCE model.

Some issues remain for the MSRM, and the main limits were identified as secondary impacts occurrence, influence of boundary conditions and limitation when applied in part of D_{m_s}. However, the frequency of these errors was limited in the $\mu - \delta$ design space, and the secondary impacts observed in this study are likely unrealistic given the absence of the fluid phase in the numerical model. The application of the presented results to other debris types is also a limitation because the data were collected using log debris, which have different geometries from other debris types like cars or shipping containers. The excluded effects of the surrounding water between the debris and the structure were expected to have limited influence on log debris impacts because these debris have small cross-section areas [26]. However, such effects may be more important in case of impacts of debris with larger cross-sections such as cars and shipping containers and may interact with the m_s effects. Furthermore, impact nonlinearities coming from structural failures often observed in post-disaster surveys, also caused by repeated impacts, might exclude the applicability of the presented methodology in these scenarios. Other limitations of the presented methodology are neglecting the log stiffness variability across its thickness and the non-consideration of the structure surface roughness, but the implications of these assumptions were expected to be not significant. In general, the limitations presented above imply that the findings of this study can be applied to log debris impacts on structures which remain in the elastic range during the impact. Nevertheless, these cases include many realistic scenarios as log debris are very common in extreme hydrodynamic event scenarios [21] and elastic impacts are valid if the structure remains in the elastic range, e.g. in the case of limited debris sizes. Investigating the effects of all these limitations and extending the range of applicability of the presented results will be carried out in future dedicated studies.

CRediT authorship contribution statement

Ghiassi Bahman: Writing – review & editing, Writing – original draft, Supervision, Project administration, Methodology, Funding acquisition, Formal analysis, Conceptualization. **De Iasio Alessandro:** Writing – review & editing, Writing – original draft, Visualization, Validation, Software, Resources, Methodology, Investigation, Formal analysis, Data curation, Conceptualization. **Milani Gabriele:** Writing – review & editing, Methodology, Conceptualization. **Briganti Riccardo:** Writing – review & editing, Writing – original draft, Supervision, Project administration, Methodology, Formal analysis, Conceptualization.

Declaration of Competing Interest

The authors declare that they have no known competing financial interests or personal relationships that could have appeared to influence the work reported in this paper. The author Gabriele Milani is an editor of this journal. In accordance with policy, Gabriele Milani was blinded to the entire peer review process.

Appendix A: Database of realistic impact scenarios

The 228 realistic impact scenarios are obtained as follows. The debris properties are fixed and equal to those given by ASCE/SEI 7–22 as minimum design load (see Section 2.2.2). The structures are defined from literature data for common masonry, concrete and XLAM walls. These data are reported in Table A1, where "ck" indicates characteristic values and "avg" indicates average values. In some cases, they are specific structures from the literature [16,3,5,8]. In other cases, they are defined by combining typical geometries, mechanical properties and boundary conditions [9,12,22,29,34,36]. In Table A1, H, W and b_s are the height, width and thickness of the walls. ρ_s and E_s are the homogenised density and Young's modulus of the walls considering possible non-uniform geometry of the materials, e.g. in case of hollow bricks. The boundary conditions types are described in Fig. A1. Moreover, the same hydrodynamic scenario assumed in [7] is used, i.e. water flow compatible with the shallow water hypothesis and in subcritical condition, with $h_w = 0.9m$, $Fr = 0.6$ and $v_w = 1.78m/s$. Based on this information, the impact position is defined at the same height as h_w and along the vertical centre line. The impact velocity v_d is assumed to be equal to v_w [24,31,32]. Only the debris impact loads are implemented in the analysis, consistently with ASCE/SEI 7–22 prescriptions that do not require such loads to be combined with other actions, e.g. the water flow loads. All structural models for the walls are represented with thick 3D elastic and homogeneous plate-like models having dimensions and mechanical properties taken from Table A1. This strategy simulates the walls at their macro-scale. Moreover, it allows to minimise the computational effort of running numerous impact simulations while maintaining accurate results in terms of out-of-plain bending response. This homogeneous modelling strategy is widely used in literature, including when analysing non-isotropic materials such as masonry [11] and XLAM [10] when suitable equivalent mechanical properties are used, as in the case of this study.

Table A1: Review of typical dimensions of walls made of different materials

Source	Material	H_s $[m]$	W_s $[m]$	b_s $[m]$	ρ_s $[kg/m^3]$	E $[MPa]$	bc	Notes
[22]	Clay brick masonry	3.05 (max)	3.05 (max)	0.1 (min)	n/a	n/a	1	Small buildings.
[16]	Clay brick masonry	2.7	8.64	0.1	1800	n/a	4	Case study from typical Dutch terraced houses.
[16]	Calcium silicate masonry	2.7	8.64	0.12	1700	n/a	4	Case study from typical Dutch terraced houses.
[16]	Concrete	2.7	8.64	0.12	2400	n/a	4	Case study from typical Dutch terraced houses.
[5]	Concrete masonry (infills)	2.8	3.6	0.9 / 0.14 / 0.19	1715 / 1363 / 1269	17500	6 / 8 / 9	Various combinations tested.
[3]	Clay masonry	2.474	5.615	0.1025	1680	12000	1	Sample of a typical masonry wall.
TMS 402/602 – 2016 [34]	Masonry (different typologies)	l/t = 20 (max)	h/t = 20 (max)	0.152 (1-storey, h = 2.74) 0.204 (residential) 0.305 (general)	n/a	$700\sigma_{c0}$ (clay) $900\sigma_{c0}$ (concrete)	n/a	Empirical rules for masonry design.
[8]	Hollow-clay brick masonry (infills)	2.4–4.55	2.76–6.30	0.12–0.45	n/a	494–8100	n/a	Database of 60 tested masonry infill walls.
[29]	Masonry (infills, different typologies)	n/a	n/a	n/a	n/a	n/a	1 / 5 / 6 / 7 / 8 / 9	Database of 58 tested masonry infill walls. Source of typical bc.
[12]	Hollow-clay brick masonry (infills)	n/a	n/a	n/a	694 – 788	n/a	n/a	Typical density of hollow-clay bricks.
(dimensions.com, 2023)	Solid concrete	1.83–7.92	1.22–9.75	0.09–0.4	n/a	n/a	n/a	Typical concrete wall dimensions.
[36]	XLAM	3.5 (max)	13.5 (max)	0.06–0.3	350 (ck) 420 (avg)	7400 (ck) 11000 (avg)	2 / 5	Typical properties of XLAM panels.

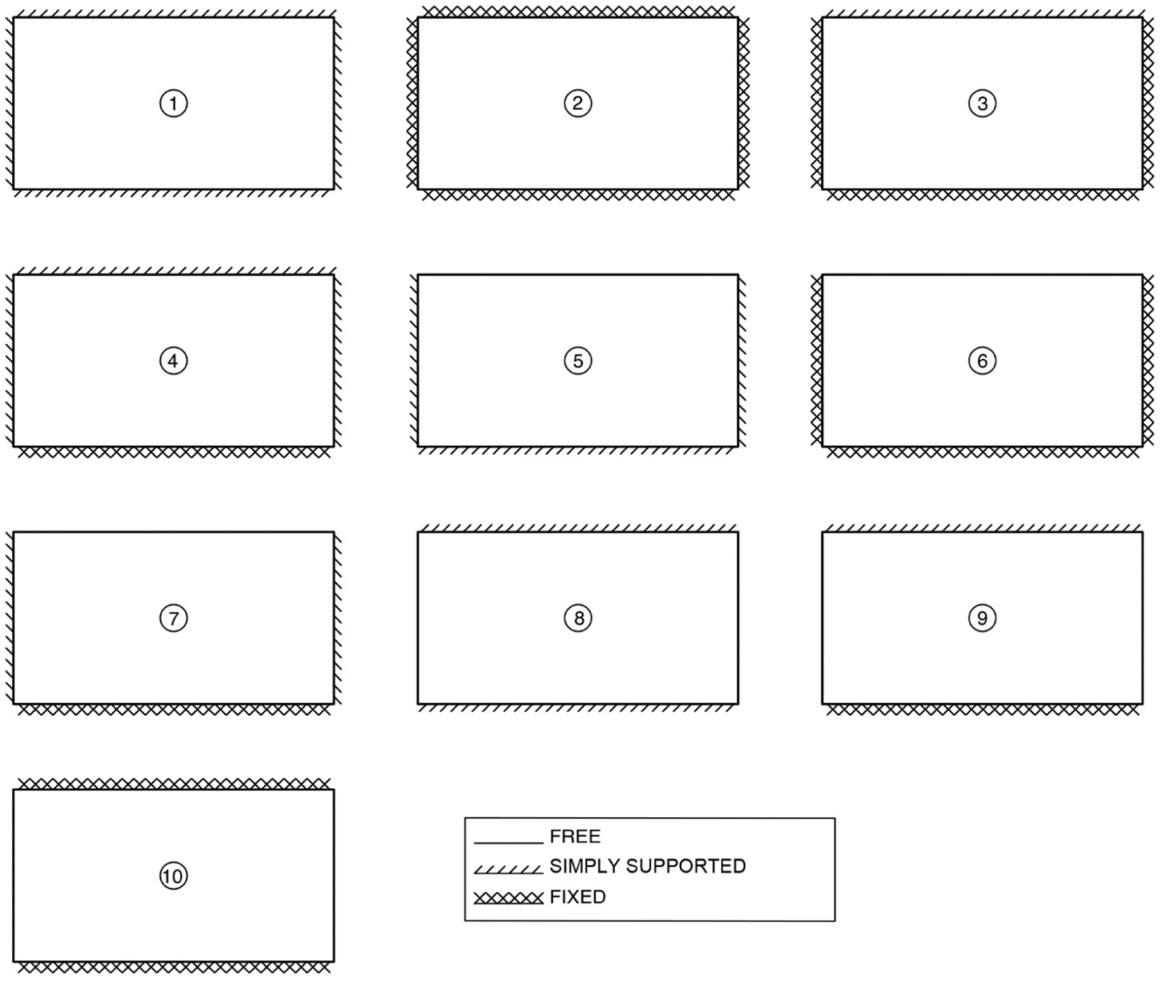

Fig. A1: Different types of boundary conditions.

Appendix B: The 1DWP model and its adaptation in ASCE/SEI 7–22

The One-Dimensional Wave Propagation (1DWP) model has been proposed by Paczkowski et al. [26] to compute the F-t diagram of log debris impacts on rigid (rigid1DWP, see Fig. B1-a) or flexible massless (flex1DWP, see Fig. B1-b) structures. The name of the model is linked to the application of the 1D elastic wave theory to describe the elastic stress wave propagation in the debris after the impact. Such a wave theory is used to compute the impact F-t diagram. The debris is modelled as an elastic, uniform, homogeneous bar that impacts the structure orthogonally. The applied wave equation is:

$$\frac{\partial^2 u(x,t)}{\partial t^2} - c_{1D}^2 \frac{\partial^2 u(x,t)}{\partial x^2} = 0 \tag{17}$$

where $u(x,t)$ is the debris displacement field, t is the time variable, and x is the axial debris coordinate with the origin at the impact side (Fig. B1). Moreover, $c_{1D} = \sqrt{E_d/\rho_d}$ is the wave speed in one dimension model, with E_d being the debris Young's modulus and ρ_d the debris density. The debris has a length L_d, cross-section area A_d and stiffness $k_d = E_d A_d / L_d$. For the flex1DWP, the structure is represented as an elastic spring with stiffness k_s. The debris hits the structure at velocity v_d. Following the well-known Hook's law and considering the debris axial force positive if compressive, the impact force F is defined as the external axial force that equilibrates the internal debris axial force at the infinitesimal debris segment in contact with the structure and deforms due to the impact action. The impact force $F(0,t)$ is computed as:

$$F(0,t) = -k_d \frac{\partial u(0,t)}{\partial t} \tag{18}$$

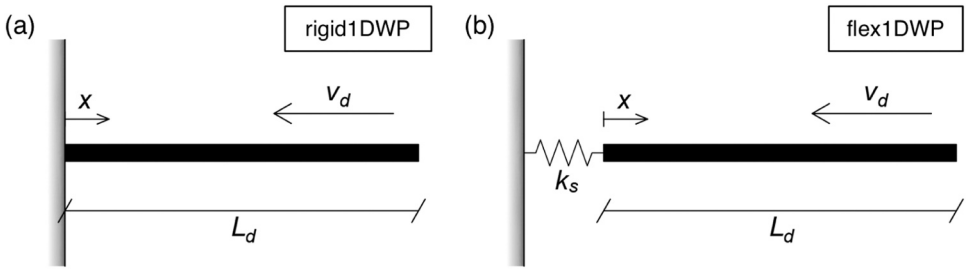

Fig. B1. Structural scheme of the 1DWP model for (a) rigid structure and (b) flexible structure

Paczkowski et al. [26] provide the solution for the related nondimensional problem. The nondimensional parameters are $\bar{u} = u/L_d$, $\bar{x} = x/L_d$, $\bar{t} = tc_{1D}/L_d$, $\bar{v}_d = v_d/c_{1D}$ and $\bar{F} = Fc_{1D}/(E_d A_d v_d)$. The stiffness ratio $\delta = k_s/k_d$ is defined. The nondimensional wave equation is:

$$\frac{\partial^2 \bar{u}(\bar{x},\bar{t}\ )}{\partial \bar{t}^2} - \frac{\partial^2 \bar{u}(\bar{x},\bar{t}\ )}{\partial \bar{x}^2} = 0 \tag{19}$$

The initial nondimensional conditions (i.e. at $\bar{t} = 0$) are $\bar{u}(\bar{x},0) = 0$, $\bar{u}_x(\bar{x},0) = -\bar{v}_d$. The first equation represents the undeformed initial state of the debris body, while the second one the uniform initial velocity of the debris body, with the minus sign needed to indicate that the velocity is negative in the adopted reference system shown in Fig. B1. The boundary nondimensional conditions for the rigid1DWP are $\bar{u}(0,\bar{t}\ ) = 0$ and $\bar{u}_x(1,\bar{t}\ ) = 0$. The first equation ensures that the debris displacement at $\bar{x} = 0$ is null during the impact (being the structure rigid). The second equation fixes the external axial force at the free debris end as always equal to zero. The boundary nondimensional conditions for the flex1DWP are $\delta\bar{u}(0,\bar{t}\ ) - \bar{u}_x(0,\bar{t}\ ) = 0$ and $\bar{u}_x(1,\bar{t}\ ) = 0$. The first equation ensures that the force in the external spring equilibrates the axial force at the infinitesimal debris segment in contact with the structure. The second equation is the same as the rigid model.

The nondimensional solution of the rigid1DWP, obtained with the method of characteristics, is a rectangular F-t diagram, $\bar{F}(0,\bar{t}\ ) = 1$ for $\bar{t} \in (0, \bar{t}_d)$, where $\bar{t}_d$ is the nondimensional impact duration and equal to 2. The related dimensional force $F(0,t)$ is:

$$F(0,t)_{rigid1DWP} = v_d\sqrt{m_d k_d} \tag{20}$$

while the dimensional impact duration t_d is:

$$t_{d,rigid1DWP} = 2\sqrt{\frac{m_d}{k_d}} \tag{21}$$

It is worth noting that the time t_d expressed in Eq. 21 is the time needed by a longitudinal stress wave to travel along the debris length from the impact face to the opposite one and return.

Conversely, the nondimensional solution of the flex1DWP, obtained with the method of separation of variables and modal superposition based on Fourier series, is a sinusoidal F-t diagram. The nondimensional force $\bar{F}(0,\bar{t}\ )$ has equation:

$$\bar{F}(0,\bar{t})_{flex1DWP} = \sum_{n=0}^{\infty} \dot{Y}_n(0)\sin(\alpha_n \bar{t}) \tag{22}$$

where:

$$\dot{Y}_n(0) = \frac{4}{2\alpha_n\left(\frac{\alpha_n^2}{\delta^2} + \frac{1}{\delta} + 1\right) - \frac{2\alpha_n}{\delta}\cos(2\alpha_n) + \left(\frac{\alpha_n^2}{\delta^2} - 1\right)\sin(2\alpha_n)} \tag{23}$$

The coefficients α_n are the n-th solutions of the equation $\alpha_n \tan(\alpha_n) = \delta$. The value $n_{max} = 50$ is enough to achieve convergence [26]. The related dimensional force $F(0,t)$ is easily obtained by inverting the nondimensionalization relations.

The design provisions by ASCE/SEI 7–22 are based on the 1DWP model. A rectangular F-t diagram is prescribed for every value of δ. Similarly to Eq. 20, the peak force is computed as:

$$F_{ASCE} = v_d\sqrt{m_d k_{eff}} \tag{24}$$

where $k_{eff} = \min\{k_d, k_s\}$ is the effective impact stiffness, which accounts for the structure flexibility in the debris-structure interaction. Similarly to Eq. 21, the impact duration is:

$$t_{d,ASCE} = 2\sqrt{\frac{m_d}{k_{eff}}} \tag{25}$$

It is worth noting that the rigid1DWP and ASCE models coincide for $\delta \geq 1$ as Eq. 20 equals Eq. 24 and Eq. 21 equals Eq. 25 in such circumstances.

The nondimensional F-t diagrams of the rigid1DWP, flex1DWP and ASCE models are plotted in Fig. B2, which shows that the flex1DWP has a more severe loading rate and peak force and lower impact duration as δ increases, and it eventually converges to the rigid1DWP. The sinusoidal shape is lost after $\delta = 1$. The peak force of the flexible model is already 98.2% of the rigid results at $\delta = 2$, but the impact duration is 41.5% higher, and the shape is still slightly sinusoidal. The peak force equals the value of the rigid model for $\delta > 3$. The impact duration and the F-t shape are nearly the same as the rigid 1DWP ones only for $\delta > 40$, but strong similarities are found already for $\delta > 5$. Under the assumption of massless structure, these data allow to

define flexible impacts for $\delta < 1$, rigid impacts for $\delta > 5$ and intermediate impacts for $1 < \delta < 5$.

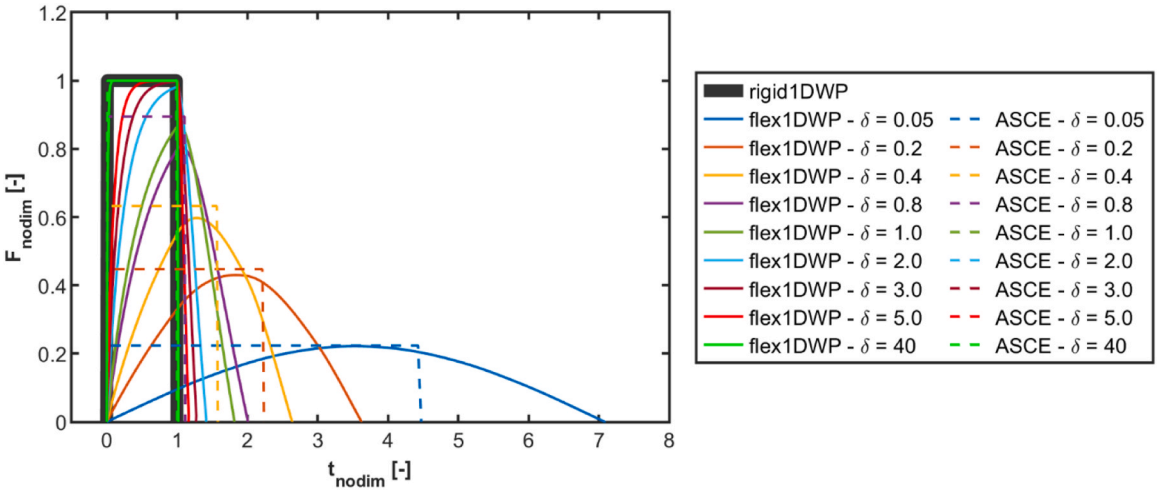

Fig. B2. Nondimensional F-t diagrams for the 1DWP and ASCE models

Similarly to the flex1DWP, also the ASCE model has a higher peak force and lower impact duration as δ increases. However, some comments can be made comparing these two models. Considering $\delta < 1$, the shape of the F-t diagrams is different, being sinusoidal for the flex1DWP model and rectangular for the ASCE model. Moreover, the ASCE maximum impact force is higher than the flex1DWP one for $\delta > 0.05$, while they are similar for $\delta < 0.05$. The ASCE impact duration is lower than the flex1DWP one, but the impulse I, i.e. the area below the diagram, is similar ($\cong$ 0.9% maximum difference). Instead, considering $\delta \geq 1$, the ASCE models equals the rigid1DWP, as mentioned above. Therefore, the same comparison between the rigid1DWP and the flex1DWP holds between ASCE and the flex1DWP.

Appendix C: General validity of the plate impact model

The impact model defined in Section 2.1 is representative of any impact scenario having the same μ and δ. This is demonstrated in Fig. C1 showing that such a model results in similar F-t diagrams when varying the structure geometry and boundary conditions, or debris geometry, while maintaining μ and δ. The impact scenario involving the SB01 masonry wall tested by Chong [3] is also analysed. This wall is 5.615m wide, 2.475m tall and 0.1025m thick and the boundary conditions are clamped base, simply supported vertical edges and free top edge. This wall can be modelled with homogeneous properties using density equal to 1680kg/m^3 and Youngs' modulus equal to 14000MPa [19]. Using the debris properties defined in Section 2.2.1, $\mu = 5.3$ and $\delta = 0.25$. An impact model with the square plate defined in Section 2.2.1 is implemented such that μ and δ are maintained, which results in a similar F-t diagram (Fig. C2). These data demonstrate the general validity of the impact models used in this study, for which the structure and debris geometrical and mechanical properties do not need to be realistic values but only lead to realistic values of μ and δ.

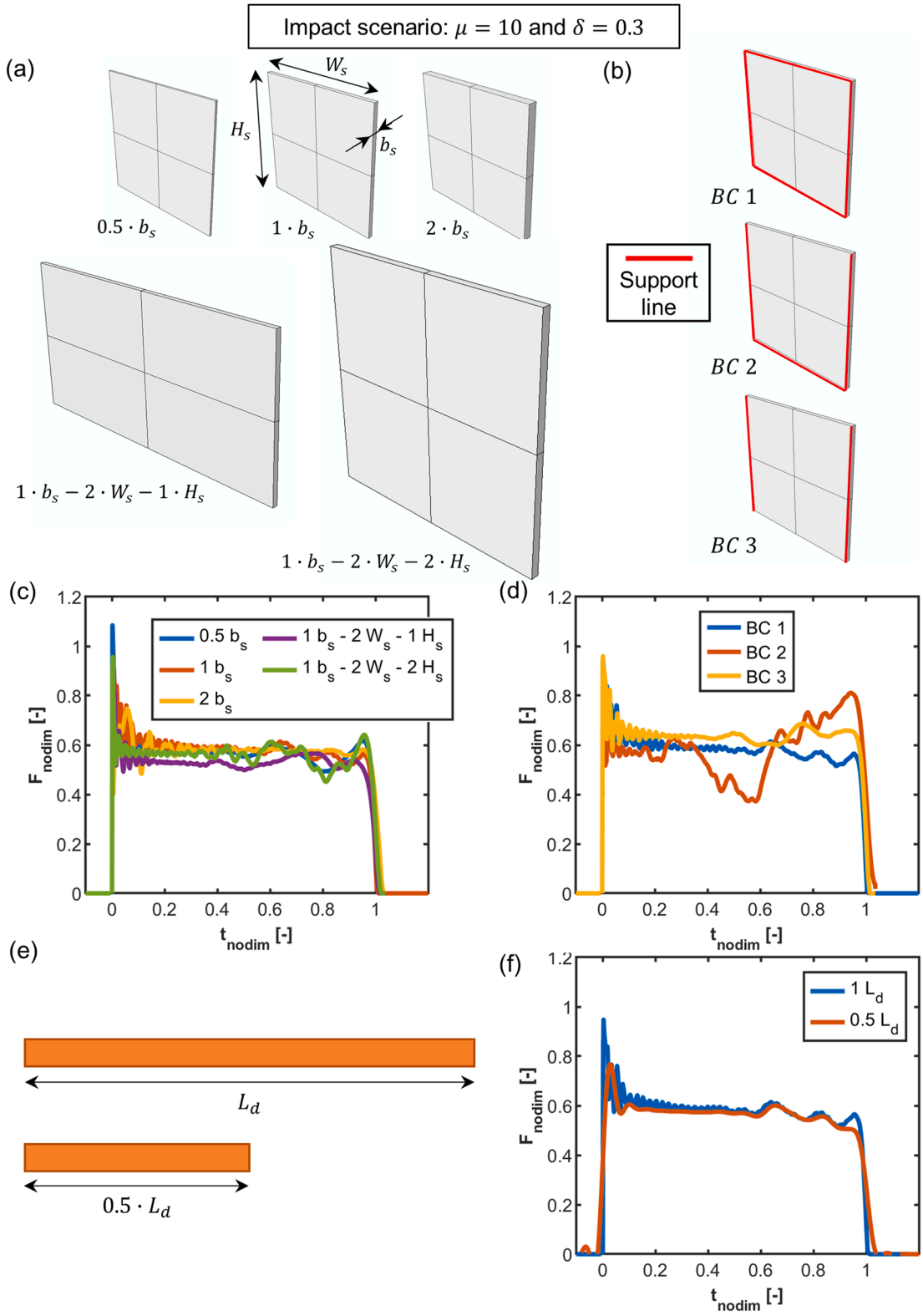

Fig. C1. Impact scenario with $\mu = 10$ and $\delta = 0.3$. Impact models and F-t diagrams with (a, c) different structure geometry and (b, d) boundary conditions. Impact models and F-t diagrams with (e, f) different debris geometry

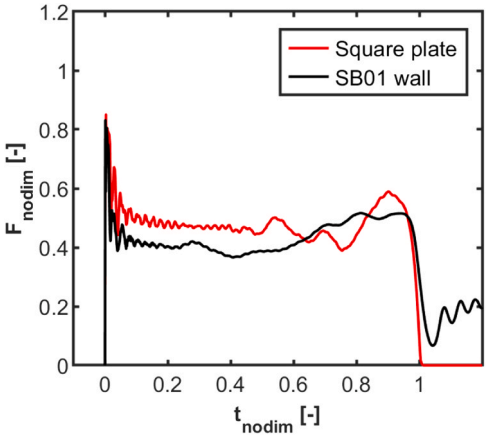

Fig. C2. F-t diagrams for the impact model with the square plate and SB01 wall

Appendix D: Values of θ_I

The values of θ_I discussed in Section 3.2 are reported in Table D1.

Table D1. Values of θ_I

Simulations	δ [−]	μ [−]	θ_I [%]	Simulations	δ [−]	μ [−]	θ_I [%]
Applied self-weight	0.4	0.1	−0.02	Vertical external loads p	0.4	20	0.03 ($p = p_1$)
	0.4	1	0.03		0.4	20	−0.05 ($p = p_2$)
	0.4	2	0.05		3	2	−0.09 ($p = p_1$)
	0.4	5	−0.01		3	2	−0.05 ($p = p_2$)
	0.4	20	0.04	Horizontal water flow loads q_w	0.4	20	−1.25 ($q_w = q_{w,1}$)
	0.4	40	−0.01		0.4	20	−1.21 ($q_w = q_{w,2}$)
	0.4	100	−0.02		3	2	−0.03 ($q_w = q_{w,1}$)
	1	2	0.01		3	2	0.26 ($q_w = q_{w,2}$)
	1	20	−0.03	Boundary conditions	0.4	20	−2.38 (bc #4)
	3	2	−0.02		0.4	20	1.49 (bc #5)
	3	20	0.02		3	2	−0.04 (bc #4)
	5	2	0.01		3	2	−6.1 (bc #5)
	5	20	−0.02				

Data Availability

Data will be made available on request.

References

[1] Abaqus. Abaqus User Manual. United States: Dassault Systèmes Simulia Corp; 2018.
[2] ASCE. Minimum Design Loads and Associated Criteria for Buildings and Other Structures. ASCE/SEI 7-22. Reston, VA; 2022.
[3] Chong VL. The Behaviour of Laterally Loaded Masonry Panels with Openings. Plymouth: University of Plymouth; 1993.
[4] Clough RW, Penzien J. Dynamics of Structures. 2nd ed. ed. New York: McGraw-Hill; 1993.
[5] Dawe JL, Seah CK. Out-of-plane resistance of concrete masonry infilled panels. Can J Civ Eng 1989;16:854–64. https://doi.org/10.1139/L89-128.
[6] De Iasio A, Ghiassi B, Briganti R. Effects of the structural mass on the waterborne debris impact force. Eng Struct 2024;318:118719. https://doi.org/10.1016/j.engstruct.2024.118719.
[7] De Iasio A, Ghiassi B, Briganti R, Milani G. High strain rate effects in masonry structures under waterborne debris impacts. Eng Struct 2023;297:116911. https://doi.org/10.1016/J.ENGSTRUCT.2023.116911.
[8] De Risi MT, Del Gaudio C, Ricci P, Verderame GM. In-plane behaviour and damage assessment of masonry infills with hollow clay bricks in RC frames. Eng Struct 2018;168:257–75. https://doi.org/10.1016/j.engstruct.2018.04.065.
[9] dimensions.com. Concrete Wall - Panel, Solid Dimensions & Drawings | Dimensions.com [WWW Document]. URL https://www.dimensions.com/element/concrete-wall-panel-solid; 2023 (Accessed 8.7.23).
[10] Franzoni L, Lebée A, Lyon F, Forêt G. Elastic behavior of Cross Laminated Timber and timber panels with regular gaps: thick-plate modeling and experimental validation. Eng Struct 2017;141:402–16. https://doi.org/10.1016/j.engstruct.2017.03.010.
[11] Ghiassi B, Milani G. Numerical modelling of masonry and historical structures: from theory to application. Numer Model Mason Hist Struct Theory Appl 2019;1:795. https://doi.org/10.1016/C2017-0-01579-3.
[12] gosmartbricks.com. Difference Between Clay Bricks Vs Hollow Clay Bricks | Go Smart Bricks [WWW Document]; 2023. (Accessed 8.7.23). URL https://gosmartbricks.com/difference-between-clay-bricks-vs-hollow-clay-bricks/.
[13] Haehnel RB, Daly SF. Maximum impact force of woody debris on floodplain structures. J Hydraul Eng 2004;130:112–20. https://doi.org/10.1061/(ASCE)0733-9429(2004)130:2(112).
[14] Ishiki K, Cunningham LS, Rogers BD. Multiphysics coupling using SPH for coastal structures subject to tsunami-driven hydrodynamic and debris impact loads. J Water Port Coast Ocean Eng 2025;151. https://doi.org/10.1061/JWPED5.WWENG-2157.
[15] Jalayer F, Aronica GT, Recupero A, Carozza S, Manfredi G. Debris flow damage incurred to buildings: an in situ back analysis. J Flood Risk Manag 2018;11:S646–62. https://doi.org/10.1111/jfr3.12238.
[16] Jansen L, Korswagen PA, Bricker JD, Pasterkamp S, de Bruijn KM, Jonkman SN. Experimental determination of pressure coefficients for flood loading of walls of Dutch terraced houses. Eng Struct 2020;216. https://doi.org/10.1016/j.engstruct.2020.110647.
[17] Kasal B. Wood formation and properties. Mechanical properties of wood. Encycl Sci 2004:1815–28. https://doi.org/10.1016/B0-12-145160-7/00041-7.
[18] Kolski H. Stress Waves in Solids. Oxford: The Clarendon Press; 1953.
[19] Lourenço P.B. An anisotropic macro-model for masonry plates and shells: implementation and validation; 1997.
[20] Majtan E, Cunningham LS, Rogers BD. Numerical study on the structural response of a masonry arch bridge subject to flood flow and debris impact. Structures 2023;48:782–97. https://doi.org/10.1016/j.istruc.2022.12.100.

[21] Naito C, Asce M, Cercone C, Asce SM, Riggs HR, Cox D. Procedure for Site Assessment of the potential for tsunami debris impact. J Water Port Coast Ocean Eng 2014;140:223–32. https://doi.org/10.1061/(ASCE)WW.1943-5460.0000222.
[22] Nash WG. Brickwork Two. Third. ed. London: Hutchinson Educational; 1969.
[23] Ngo T, Mendis P, Gupta A, Ramsay J. Blast loading and blast effects on structures – an overview. Electron J Struct Eng 7 2007:76–91. https://doi.org/10.56748/ejse.671.
[24] Nistor I, Goseberg N, Stolle J. Tsunami-driven debris motion and loads: a critical review. Front Built Environ 2017;3. https://doi.org/10.3389/fbuil.2017.00002.
[25] Nistor I, Palermo D, Nouri Y, Murty T, Saatcioglu M. Tsunami-induced forces on structures. Handb Coast Ocean Eng: Expand Ed 2018;1–2:481–506. https://doi.org/10.1142/9789813204027_0018.
[26] Paczkowski K, Riggs HR, Naito CJ, Lehmann A. A one-dimensional model for impact forces resulting from high mass, low velocity debris. Struct Eng Mech 2012;42:831–47. https://doi.org/10.12989/SEM.2012.42.6.831.
[27] Petrone C, Rossetto T, Goda K. Fragility assessment of a RC structure under tsunami actions via nonlinear static and dynamic analyses. Eng Struct 2017;136:36–53. https://doi.org/10.1016/j.engstruct.2017.01.013.
[28] Piran Aghl P, Naito CJ, Riggs HR. Full-scale experimental study of impact demands resulting from high mass, low velocity debris. J Struct Eng 2014;140:04014006. https://doi.org/10.1061/(asce)st.1943-541x.0000948.
[29] Pradhan B, Zizzo M, Sarhosis V, Cavaleri L. Out-of-plane behaviour of unreinforced masonry infill walls: review of the experimental studies and analysis of the influencing parameters. Structures 2021;33:4387–406. https://doi.org/10.1016/j.istruc.2021.07.038.
[30] Qi ZX, Eames I, Johnson ER. Force acting on a square cylinder fixed in a free-surface channel flow. J Fluid Mech 2014;756:716–27. https://doi.org/10.1017/JFM.2014.455.
[31] Ruffini G, Briganti R, Girolamo PDe, Stolle J, Ghiassi B, Castellino M. Numerical modelling of flow-debris interaction during extreme hydrodynamic events with DualSPHysics-CHRONO. 3618 11 Appl Sci 2021 2021;11:3618. https://doi.org/10.3390/APP11083618.
[32] Ruffini G, Domínguez JM, Briganti R, Altomare C, Stolle J, Crespo AJC, Ghiassi B, Capasso S, De Girolamo P. MESH-IN: a MESHed INlet offline coupling method for 3-D extreme hydrodynamic events in DualSPHysics. Ocean Eng 2023;268:113400. https://doi.org/10.1016/j.oceaneng.2022.113400.
[33] Samali B, McKenzie G, Zhang C, Ancich E. Review of the basics of state of the art of blast loading. Asian J Civ Eng 2018;19:775–91. https://doi.org/10.1007/s42107-018-0063-y.
[34] The Masonry Society. TMS 402/602 Building Code Requirements and Specifications for Masonry Structures; 2016.
[35] Wüthrich D, Korswagen PA, Selvam H, Oetjen J, Bricker J, Schüttrumpf H. Field survey assessment of flood loads and related building damage from the July 2021 event in the Ahr Valley (Germany). J Flood Risk Manag 2024. https://doi.org/10.1111/JFR3.13024.
[36] X-LAM Dolomiti. XLAM Technical Data and Documentation. Castel Ivano, Italy; 2023.